BNL-111998-2016-JA

AGU PUBLICATIONS

JGR

Journal of Geophysical Research: Atmospheres

RESEARCH ARTICLE

10.1002/2015JD024446

Key Points:
- Azimuthally averaged scanning polarimetric radar data reveal episodic melting layer sagging
- Aircraft data show denser, faster-falling particles (from riming in one case) lead to the signature
- A bin model of melting snow with varying rime fraction reproduces the observed radar signatures

Correspondence to:
M. R. Kumjian,
kumjian@psu.edu

Citation:
Kumjian, M. R., S. Mishra, S. E. Giangrande, T. Toto, A. V. Ryzhkov, and A. Bansemer (2016), Polarimetric radar and aircraft observations of saggy bright bands during MC3E, *J. Geophys. Res. Atmos.*, *121*, 3584–3607, doi:10.1002/2015JD024446.

Received 3 NOV 2015
Accepted 14 MAR 2016
Accepted article online 19 MAR 2016
Published online 14 APR 2016

©2016. American Geophysical Union. All Rights Reserved.

Polarimetric radar and aircraft observations of saggy bright bands during MC3E

Matthew R. Kumjian[1], Subashree Mishra[2,3], Scott E. Giangrande[4], Tami Toto[4], Alexander V. Ryzhkov[3,5], and Aaron Bansemer[6]

[1]Department of Meteorology, Pennsylvania State University, University Park, Pennsylvania, USA, [2]U.S. Department of Energy, Washington, District of Columbia, USA, [3]NOAA/OAR National Severe Storms Laboratory, Norman, Oklahoma, USA, [4]Atmospheric Sciences Division, Brookhaven National Laboratory, Upton, New York, USA, [5]Cooperative Institute for Mesoscale Meteorological Studies and the University of Oklahoma, Norman, Oklahoma, USA, [6]Mesoscale and Microscale Meteorology Division, National Center for Atmospheric Research, Boulder, Colorado, USA

Abstract Polarimetric radar observations increasingly are used to understand cloud microphysical processes, which is critical for improving their representation in cloud and climate models. In particular, there has been recent focus on improving representations of ice collection processes (e.g., aggregation and riming), as these influence precipitation rate, heating profiles, and ultimately cloud life cycles. However, distinguishing these processes using conventional polarimetric radar observations is difficult, as they produce similar fingerprints. This necessitates improved analysis techniques and integration of complementary data sources. The Midlatitude Continental Convective Clouds Experiment (MC3E) provided such an opportunity. Quasi-vertical profiles of polarimetric radar variables in two MC3E stratiform precipitation events reveal episodic melting layer sagging. Integrated analyses using scanning and vertically pointing radar and aircraft measurements reveal that saggy bright band signatures are produced when denser, faster-falling, more isometric hydrometeors (relative to adjacent times) descend into the melting layer. In one case, strong circumstantial evidence for riming is found during bright band sagging times. A bin microphysical melting layer model successfully reproduces many aspects of the signature, supporting the observational analysis. If found to be a reliable indicator of riming, saggy bright bands could be a proxy for the presence of supercooled liquid water in stratiform precipitation, which may provide important information for mitigating aircraft icing risks and for constraining microphysical models.

1. Introduction

In cold clouds, growth from freshly nucleated ice crystals to precipitation-sized particles follows a number of pathways involving some combination of vapor deposition, aggregation, and riming. The conditions favorable to each of these microphysical processes are substantially different; for example, riming requires supercooled liquid droplets coexisting with ice crystals, whereas aggregation can occur given sufficient numbers of crystals with particular habits and/or sticking coefficients. Owing to the differences in these microphysical processes, a given population of pristine ice particles may eventually precipitate out of the cloud with dramatically varied sizes, densities, and fall speeds, ultimately affecting the ice mass flux out of the cloud and the surface precipitation distribution. Thus, understanding when and where these processes are acting and under what conditions they may be dominant is critical for simulating realistic cloud behavior and life cycles in numerical models.

Largely due to a lack of routine in situ observations and field campaigns, remote sensing platforms often are used to gain insights into cloud microphysical processes as well as to provide observational constraints for model representations of these processes. In particular, polarization diversity radars can be particularly helpful in diagnosing ongoing microphysical processes in precipitation. This is because polarimetric radar measurements provide valuable information about particle sizes, shapes, composition, and orientations (e.g., see reviews by *Herzegh and Jameson* [1992], *Doviak and Zrnić* [1993], *Zrnić and Ryzhkov* [1999], *Bringi and Chandrasekar* [2001], *Ryzhkov et al.* [2005], *Kumjian* [2013a, 2013b, 2013c], among others). These measurements include reflectivity factor at horizontal polarization Z_H, differential reflectivity Z_{DR}, differential propagation phase shift Φ_{DP} and half its range derivative specific differential phase K_{DP}, linear depolarization ratio LDR, and the copolar correlation coefficient ρ_{hv}. Such measurements have been used in recent studies

to explore various microphysical processes in cold clouds, including snow and ice melting [e.g., *Ryzhkov et al.*, 2013a, 2013b, *Trömel et al.*, 2014], vigorous dendritic crystal growth [e.g., *Kennedy and Rutledge*, 2011; *Andrić et al.*, 2013; *Bechini et al.*, 2013; *Schrom et al.*, 2015], secondary ice crystal production [e.g., *Hogan et al.*, 2002; *Oue et al.*, 2015b], and freezing of partially or fully melted hydrometeors into ice pellets [*Kumjian et al.*, 2013; *Kumjian and Schenkman*, 2014].

Of particular interest in the present study are aggregation and riming processes as observed in midlatitude, continental, mixed-phase cloud systems. Both processes contribute to ice hydrometeor growth and changes in particle fall speeds, which ultimately affect precipitation fluxes. However, there are important microphysical differences between the two processes that must be distinguished. For example, aggregation does not necessarily indicate liquid water, whereas riming does. Designating cloud regions with ongoing riming or aggregation will help distinguish regions with different microphysical, radiative, and thermodynamic properties. Such designations are important for constraining new microphysical parameterization schemes that predict properties of ice particles grown by these processes [e.g., *Morrison and Milbrandt*, 2015; *Morrison et al.*, 2015; *Jensen and Harrington*, 2015]. In addition, there are obvious practical implications for detecting supercooled liquid water in clouds (such as potential aviation hazards).

Very often, heavily rimed crystals and aggregates have scattering properties that render them nearly indistinguishable when observed with scanning polarimetric radars at longer wavelengths (e.g., S, C, and X bands) that are used most frequently in operations. Owing to their larger sizes, aggregates produce relatively larger Z_H at longer radar wavelengths than pristine ice crystals. In addition, their relatively low apparent density and more chaotic orientations result in lower Z_{DR}. Similarly, graupel particles tend to be characterized by larger Z_H and very low Z_{DR} compared to pristine ice. Both graupel and aggregates generally contribute little to Φ_{DP}, whereas it can accumulate as the radar wave propagates through high concentrations of pristine ice crystals. Thus, the transformation from pristine ice to aggregates or to graupel in clouds will generally produce very similar polarimetric radar fingerprints given traditional data interrogation techniques [e.g., *Kumjian et al.*, 2014; *Vogel et al.*, 2015].

Effectively identifying potentially subtle differences in these microphysical fingerprints requires alternative means to analyze radar data and/or additional measurements from independent instruments. In this study, we integrate data from scanning dual-polarization radar with in situ aircraft measurements collected during the Midlatitude Continental Convective Clouds Experiment (MC3E) [*Jensen et al.*, 2016], a joint effort between the U.S. Department of Energy (DOE) Atmospheric Radiation Measurement (ARM) Program and the National Aeronautics and Space Administration Global Precipitation Measurement (GPM) mission [*Hou et al.*, 2014] that took place at the ARM Climate Facility at the Southern Great Plains (SGP) site in northern Oklahoma [*Mather and Voyles*, 2013] from 22 April to 6 June 2011. We document and describe a polarimetric radar-based signature of denser, faster-falling particles that in at least one case is associated with riming. The signature is observed as a transient sagging of the melting layer bright band in time-height profiles of azimuthally averaged polarimetric radar variables. Further, we use profiling radar and in situ aircraft data to complement the scanning radar-based inferences and use a bin microphysical model to reproduce and explain the underlying physics leading to the sagging bright band signature. The next section presents an overview of the cases and data set. Section 3 presents the analysis technique for the scanning polarimetric radar data used in this study. Section 4 provides an analysis of these data, followed by supporting results from a simple one-dimensional microphysical model in section 5. A discussion and summary of the main conclusions are found in section 6.

2. MC3E Data Set

Convective storms occurring on 27 April and 20 May 2011 are the focus of this study. These storms were well sampled during MC3E, taking place over the DOE ARM SGP Climate Research Facility. Figure 1 presents an overview of both events in the form of time-height evolution plots of mean Doppler velocity from the ultrahigh-frequency (UHF; 32.8 cm wavelength) vertically pointing radar wind profiler (RWP) at the SGP site [e.g., *Giangrande et al.*, 2013]. These column depictions can provide useful insights into storm microphysical processes over the SGP site; however, new scanning radar capabilities were introduced for the MC3E campaign to provide improved spatial, temporal, and microphysical (via dual polarization and additional radar wavelength diversity) storm observations. This unique combination of ground-based, remote sensing, and aircraft-mounted observational systems makes MC3E an ideal field campaign to study microphysical processes in convective storms.

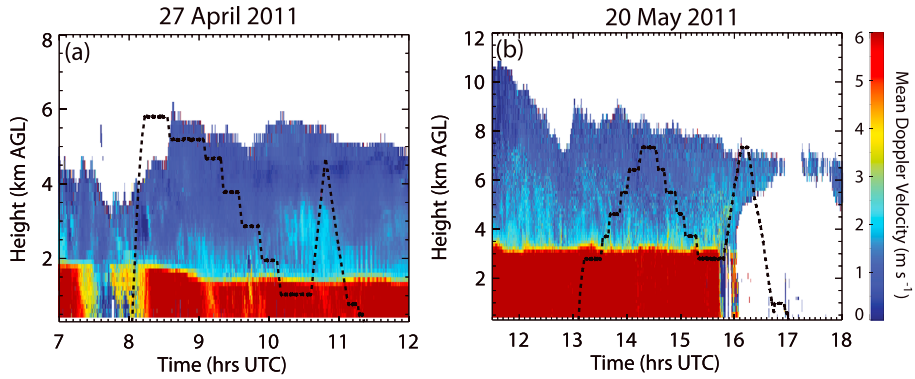

Figure 1. Time-height plots of the mean Doppler velocity observed by the ultrahigh-frequency (UHF) ARM vertically pointing radar wind profiler (RWP) at the SGP site during the (a) 27 April 2011 and (b) 20 May 2011 events. Note the different scales used on the abscissa and ordinate axes. For reference the associated aircraft altitude is overlaid (although this is not indicative of the aircraft specifically over the SGP facility).

Radar data serving as the focus of this study come from the polarimetric C-band Scanning ARM Precipitation Radar (CSAPR). CSAPR is a C band (6.25 GHz) polarimetric radar operating in a mode of simultaneous transmission and simultaneous reception of horizontally and vertically polarized electromagnetic waves. Its magnetron transmitter produces a peak power of about 350 kW. It has a 4.2 m parabolic reflector antenna that provides a 3 dB beamwidth of 0.9°. During MC3E, it operated under standard ~5–6 min volume coverage patterns comprising multitilt PPI (surveillance) scans, as well as range-height indicator (RHI) scans directed over the ARM SGP Central Facility (CF). CSAPR is located ~21.5 km north-northeast of the CF. The absolute radar calibration was ensured for CSAPR to within 1–2 dB during the campaign [*Giangrande et al.*, 2014]. For the 27 April case, 1.4 dB was subtracted from the raw Z_{DR} fields to approximately correct for a positive bias. Of most importance in the present study is the relative spatiotemporal patterns in the radar fields, not the absolute values therein. Thus, the stated calibrations are sufficient for our purposes.

Aircraft data from the University of North Dakota (UND) Citation are used herein and include a number of cloud microphysical, particle imaging, and thermodynamic probes. These probes provide estimates of cloud liquid and ice water contents, particle types, sizes, and distributions, as well as standard meteorological quantities such as temperature, moisture, and air vertical velocities. Data from these instruments are used to compare in-cloud microphysical phenomena with observations from the ground-based scanning polarimetric radars.

Flight-level vertical velocities shown herein are calculated from the vertical component of the wind speed and were provided by UND scientists. The relative humidity was calculated from the dewpoint temperature and water vapor mixing ratio measured by the aircraft. The wet-bulb temperature was calculated using an empirical formula from *Stull* [2011].

The microphysical measurements during MC3E are described in *Wang et al.* [2015]. Briefly, ice particle size distributions (PSDs) were produced from combined spectra measured by the Particle Measuring System 2-Dimensional Cloud (2DC) probe and the High Volume Precipitation Spectrometer (HVPS-3) made by Stratton Park Engineering Company, Inc. [*Lawson et al.*, 1998]. The 2DC probe [*Knollenberg*, 1981] is an optical array probe with 30 μm size resolution, whereas the HVPS-3 probe has 150 μm resolution. In addition to the 2DC and HVPS-3, the Cloud Imaging Probe (CIP) from Droplet Measurement Technologies (DMT) was used to examine high-resolution ice crystal images in the size range 100 μm to 1.55 mm, at 25 μm resolution. The DMT Cloud Droplet Probe (CDP) captures the number concentration of small particles with sizes less than 50 μm; hence, it indicates the presence of supercooled liquid water droplets and small ice particles. The Citation was also outfitted with a Rosemount icing detector [e.g., *Cober et al.*, 2001] that detects the presence of supercooled liquid water.

Besides these direct probe measurements, an important derived parameter used in this study is the area ratio (AR) [*Heymsfield and Westbrook*, 2010, among others]. The AR is defined as the ratio of the projected area of the two-dimensional ice crystal image to the area of a circumscribed circle. AR values near unity imply spherical particles, whereas lower values imply nonspherical particles. The AR for the MC3E microphysical probe data was calculated from the HVPS-3 alone (i.e., not based on combined spectra from the 2DC and HVPS-3).

Environmental conditions differed considerably between the two events studied herein. On 27 April 2011, widespread stratiform precipitation with embedded convection developed over the CF in association with an upper level low passage. Following surface cyclogenesis and a cold front passage, strong low-level winds backed from easterly to northerly by about 1500 UTC, whereas aloft (up to 500 hPa) the winds veered from southwesterly at 0600 UTC to northwesterly. A complementary analysis of aircraft spirals and associated vertically pointing radar signatures from this event is found in (S. E. Giangrande et al., Insights into riming and aggregation processes as revealed by aircraft, radar and disdrometer observations for the 27 April 2011 widespread precipitation event, submitted to *Journal of Geophysical Research*, 2016). In contrast, 20 May 2011 featured a classic setup for deep convection, with a potent upper level trough over the mountain west and an associated cold front and dry line in the western Texas panhandle, and a low-level jet advecting warm, moist air over Oklahoma. A classic mesoscale convective system formed along the cold front and pushed through the CF during the early morning hours, trailed by a robust stratiform region. Despite the storms occurring in different environmental contexts, both featured widespread and long-lived stratiform precipitation over the CF (Figure 1). The microphysical processes above the melting layer in those stratiform regions are of interest for this study.

3. Quasi-vertical Profiles

Elucidating any subtle differences between aggregation and riming fingerprints in polarimetric radar data is difficult using traditional PPI and RHI radar scans [e.g., *Kumjian et al.*, 2014; *Vogel et al.*, 2015]. In part, this obfuscation is because short dwell times common to operational and some research radars lead to noisy estimates of the polarimetric radar variables. To alleviate these problems, we adopt "quasi-vertical profiles" (hereafter QVPs) [*Kumjian et al.*, 2013; *Trömel et al.*, 2013, 2014; *Ryzhkov et al.*, 2016], which involve azimuthal averaging of traditional PPI scans. Such azimuthal averaging over all 360° dramatically reduces the variance of the polarimetric radar variable estimates, reducing statistical errors by up to a factor of $360^{1/2}$ [*Ryzhkov et al.*, 2016].

Ryzhkov et al. [2016] suggest that elevation angles between about 10° – 20° are optimal for these methods, as these tilts provide high spatial resolution and minimize beam broadening. Furthermore, the intrinsic polarimetric contrasts of precipitation particles do not decrease significantly if the elevation angle remains below about 20° – 30° [e.g., *Bringi and Chandrasekar*, 2001]. Thus, QVPs provide a good indication of the dominant microphysical processes ongoing in a spatially averaged representative column above the radar. Time series of QVPs also provide a time-height product that may be useful for comparisons with microphysical process column models, as shown later. QVPs collapse the complexity of three-dimensional storms, reducing some of the natural variability and heterogeneities of the precipitation and revealing the dominant signals related to microphysical processes.

Obtaining the vertical precipitation structure from conventional conical scans is one of the benefits of the QVP approach. This is especially useful in the vicinity of the ARM SGP facility, in which many instruments are vertically pointing (S. E. Giangrande et al., submitted manuscript, 2016). As a complement to vertically pointing radar insights, QVP methods retain bulk dual-polarization insights at close proximity, while potentially minimizing variability produced in vertically pointing radar measurements by fall streaks and/or size sorting coupled with storm motions [e.g., *Fabry et al.*, 1992; *Mittermaier et al.*, 2004; *Szyrmer and Zawadzki*, 2014; *Oue et al.*, 2015a]. However, small-scale features within the conical scan being averaged can be washed out, and thus, certain microphysical process fingerprints may be reduced in magnitude because of this averaging. Advantages of the QVP approach over other methods of interrogating scanning radar data vertical structure such as frequency distributions [e.g., *Black et al.*, 1991, 1996; *Yuter and Houze*, 1995] include (i) QVPs retain the native "vertical" resolution of the radar measurements (i.e., no binning is required), (ii) QVPs allow for the temporal variation of the microphysical signatures to be revealed, and (iii) QVPs provide a time-height product over the radar site that can be easily compared to collocated vertically pointing instruments and one-dimensional microphysical model output. Because of these advantages, we will make use of such QVPs herein.

Quasi-vertical profiles were constructed from CSAPR data collected during the two MC3E cases. Azimuthal averaging was performed over all 360° on PPI scans at 21.4° elevation. The results herein are insensitive to using different elevation angles (QVPs were constructed using elevation angles from 5° to 45° with no

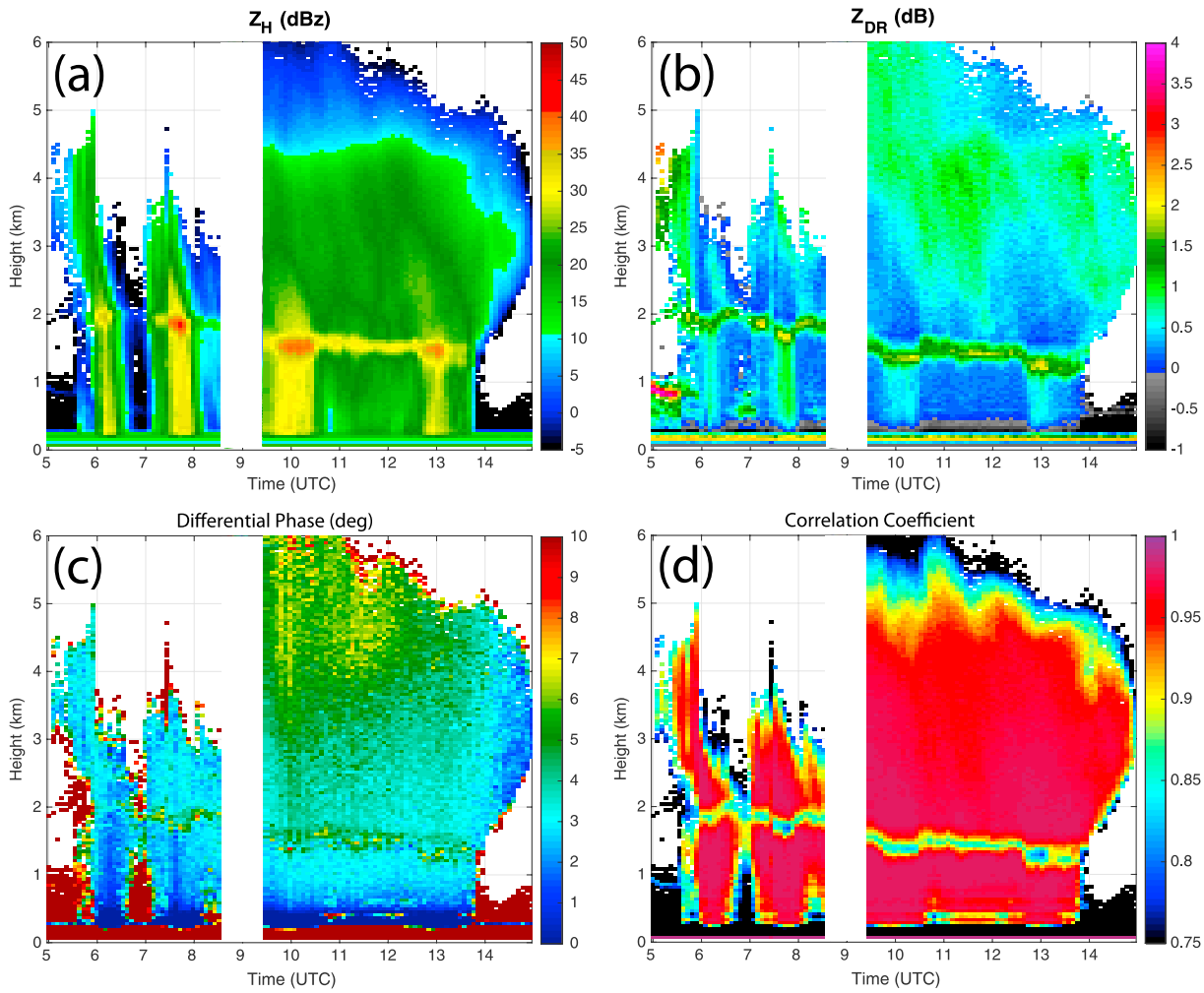

Figure 2. Time series of quasi-vertical profiles from 27 April 2011, 05:00 UTC through about 15:00 UTC. Data were collected using the CSAPR at the ARM Southern Great Plains site during MC3E. Profiles were constructed from the 21.4° elevation angle PPI scans. Data shown are (a) Z_H, (b) Z_{DR}, (c) Φ_{DP}, and (d) ρ_{hv}. The white bar indicates missing data.

qualitative differences in the signatures presented herein). See *Ryzhkov et al.* [2016] for more details on the QVP technique.

4. Results

4.1. 27 April 2011 CSAPR Analysis

Consecutive QVPs of Z_H, Z_{DR}, Φ_{DP}, and ρ_{hv} shown in a time-height plot (Figure 2) for the 27 April 2011 case reveal area-averaged vertical precipitation structure throughout the event. White vertical bars are gaps in the data when the scanning strategies were changed or data are missing. A well-defined melting layer bright band is evident in all fields, initially at about 2 km above ground level (agl). The melting layer then descends to near 1.5 km by 1000 UTC owing to low-level cold air advection by the northerly winds associated with the surface low and behind the cold front. Enhanced Z_{DR} and Φ_{DP} values aloft (>3.0 km agl) indicate pristine (nonspherical) ice crystals. The Z_{DR} maxima are found at about 4.0–4.5 km agl, close to the sounding-observed −15°C level (not shown), which suggests planar crystal habits [e.g., *Bailey and Hallett*, 2009; *Lamb and Verlinde*, 2011]. Below this level, Z_{DR} decreases and Z_H increases, implying particle growth by aggregation.

There are noticeable bright band enhancements in Z_H at several times (just before 0800 UTC, and centered at about 1000 and 1300 UTC). These features are collocated with slight depressions in the melting layer height particularly evident in Z_{DR} and ρ_{hv}, and associated with enhanced Z_H values just above and below the melting layer. In addition, Z_{DR} is noticeably lower just above the melting layer and enhanced beneath it. ρ_{hv} also is slightly lower in these enhancements than elsewhere in the melting layer.

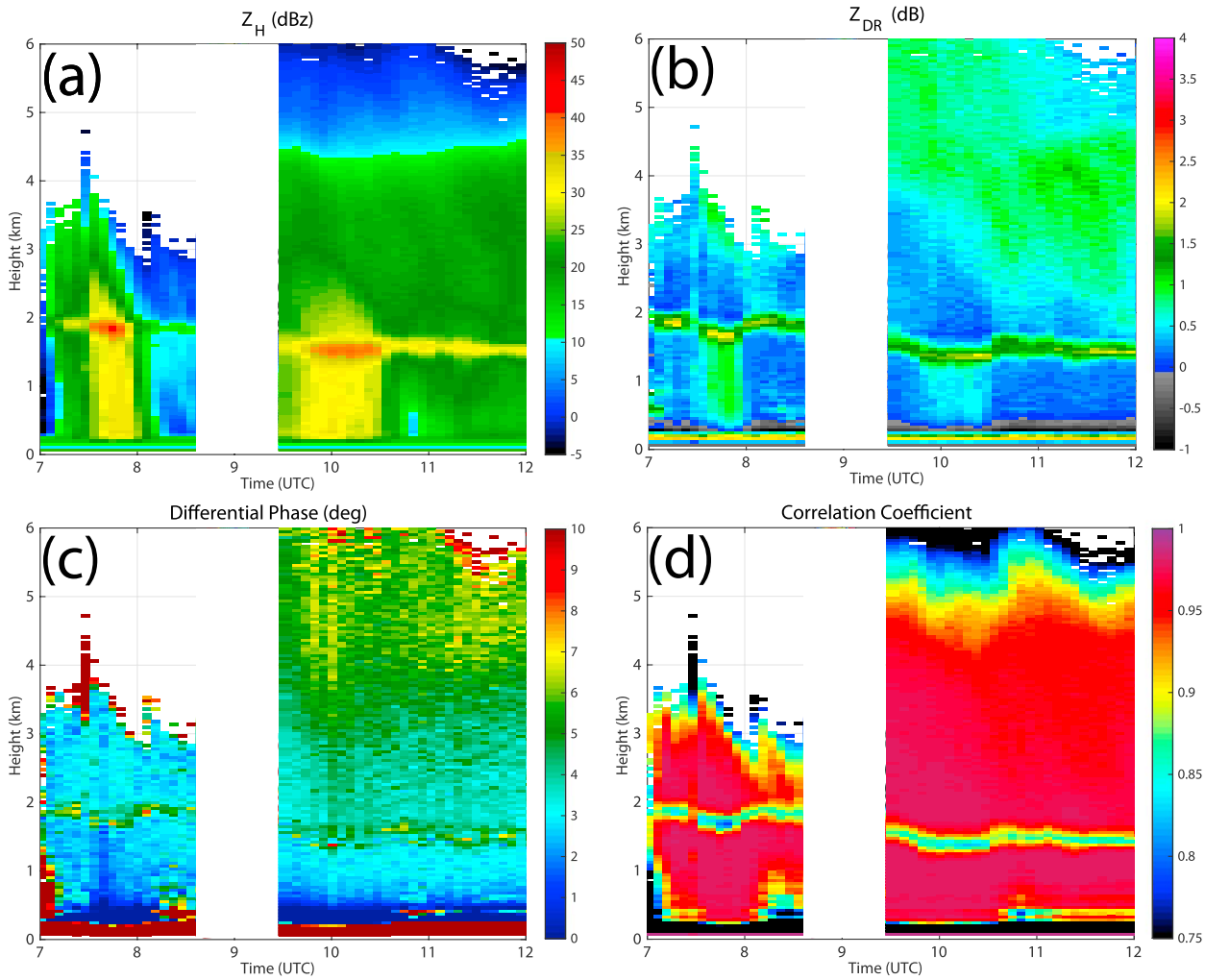

Figure 3. As in Figure 2, but zoomed in to the approximate times of the aircraft measurements. Fields shown are (a) Z_H, (b) Z_{DR}, (c) Φ_{DP}, and (d) ρ_{hv}.

Figure 3 provides a close-up view of the period encompassing the first two of these melting layer enhancements. UND Citation aircraft measurements were made during this time, from shortly after 0800 UTC through 1122 UTC [see *Wang et al.*, 2015]. Features in the ice portion of the cloud slope down and to the right. Recall these data are averaged over all azimuths, so the preferential directionality suggests precipitation particle fall streaks not biased by storm motion (which can affect vertically pointing radar observations). Thus, one can trace the enhanced Z_H above the melting layer to the enhancements within the melting layer, indicating a flux into the melting layer of larger and/or denser ice particles. The Z_H in the underlying rain (Figure 3a) similarly is enhanced over the adjacent values, consistent with the presence of relatively larger melting particles above. Similarly, Z_{DR} structures are seen in Figure 3b that seem to be correlated above, within, and below the melting layer. The ρ_{hv} is >0.97 above and below the melting layer in these enhancements (Figure 3c), though within the melting layer values are reduced compared to more quiescent times, with some values <0.85. The bright band enhancements are associated with slightly thicker reduced ρ_{hv} regions, implying that the layer containing mixed-phase melting particles occupies a greater depth during these times.

4.2. 20 May 2011 CSAPR Analysis

A similar analysis is conducted for the 20 May 2011 case (Figure 4). From about 1000–1100 UTC, the convective line moved over the radar site, leading to strong attenuation in Z_H, differential attenuation in Z_{DR}, and large Φ_{DP} accumulations. Following the squall line, heavy stratiform rain fell for a few hours. Within this stratiform region, similar sagging melting layer features are observed, associated with comparable enhancements in Z_H and Z_{DR} (and a reduction in ρ_{hv}), analogous to the 27 April 2011 case. Above these sagging melting layers,

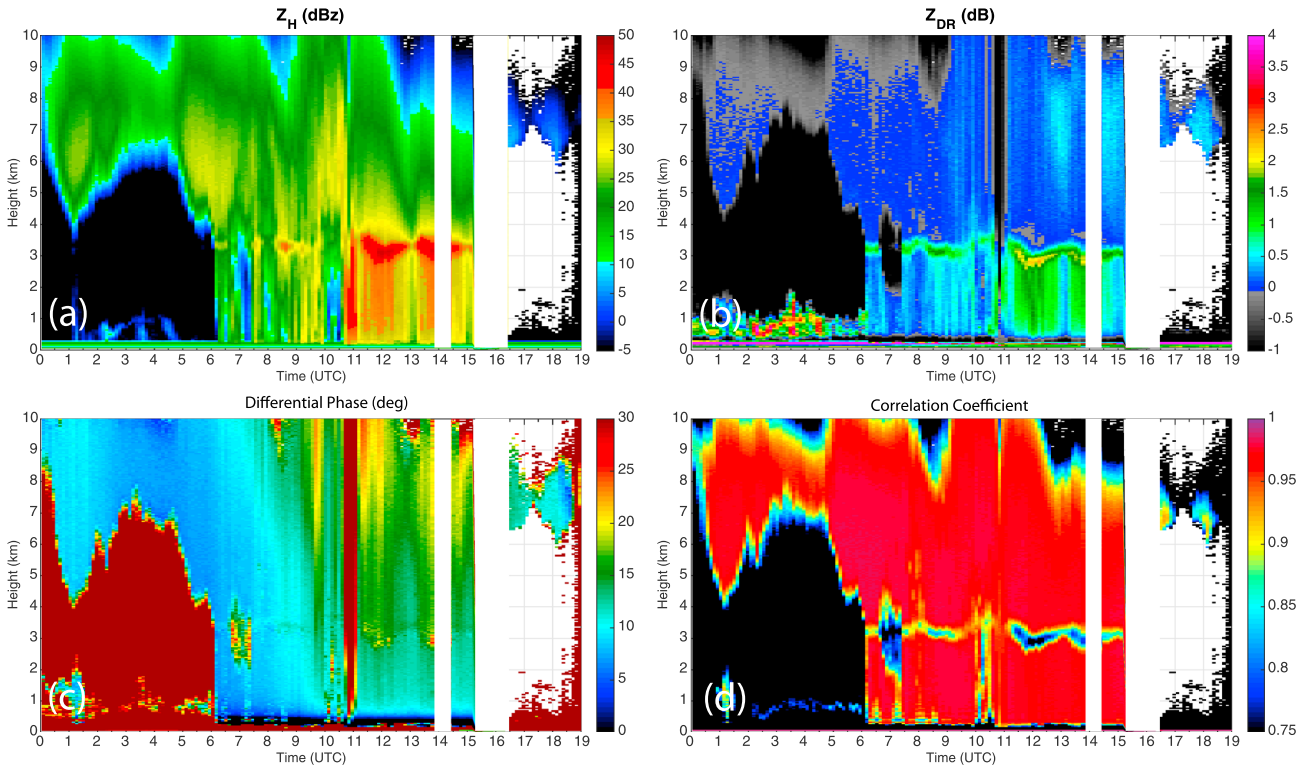

Figure 4. Time series of CSAPR QVPs from 20 May 2011, starting at 00:00 UTC. Fields shown are (a) Z_H, (b) Z_{DR}, (c) Φ_{DP}, and (d) ρ_{hv}.

one again finds enhanced Z_H and reduced Z_{DR}. Below, Z_H and Z_{DR} are enhanced over adjacent regions. Localized increases in Φ_{DP} are found during these sagging melting layer times, along with substantially reduced ρ_{hv}. The monotonic increases in Φ_{DP} with height are associated with positive specific differential phase K_{DP}. Occasionally, nonmonotonic "blips" in Φ_{DP} values are observed between about 11 and 14 UTC. These are a manifestation of an additional differential phase shift between the horizontally and vertically polarized signals produced on backscatter. Such backscatter differential phase (hereafter δ) generally may occur when large (compared to the radar wavelength), wet, nonspherical hydrometeors are present [e.g., *Trömel et al.*, 2013, and references therein]. In scanning polarimetric radar measurements, δ is observed as a "blip" in radial Φ_{DP} profiles; therefore, in QVPs, it is observed as a blip in the time-height profiles of Φ_{DP}.

Focusing in during the aircraft measurement period (Figure 5), one finds similar details in the signatures as compared to those observed on 27 April. The bright band is stronger in this case, having maximum $Z_H > 45$ dBZ and minimum $\rho_{hv} < 0.75$. Note that these extremes are obtained after azimuthal averaging, and thus, the actual extrema likely are larger in magnitude. Additionally, the vertical extent of precipitation echoes is much taller in this case compared to 27 April 2011, suggesting more ice water content and greater depths for potential growth of ice particles. Maximum QVP Z_H, Z_{DR}, and minimum QVP ρ_{hv} values in the 2–4 km height layer are selected for times from 1200 to 1400 UTC. The three-dimensional scatterplot (Figure 6) shows a strong correlation between the melting layer extrema, with stronger correlation magnitudes in this case compared to 27 April (not shown). Specifically, Z_H and Z_{DR} extrema are positively correlated, whereas both are negatively correlated with ρ_{hv}, consistent with the findings of *Vogel et al.* [2015]. This suggests that similar physical processes lead to these observed extrema.

4.3. Discussion of CSAPR Analyses

Evolution of melting layer characteristics reveals similarities between the two cases. Enhanced Z_H above, within, and below the melting layer strongly suggests the presence of larger and/or denser particles falling into the warmer air and subsequently melting, eventually becoming larger raindrops. The latter inference is verified by the enhanced Z_{DR} in rain beneath these melting layer enhancements. This indicates wider ice mass spectra aloft at times of sagging, which may arise from processes adding mass to existing particles (e.g., riming and deposition) or increasing particle number concentration.

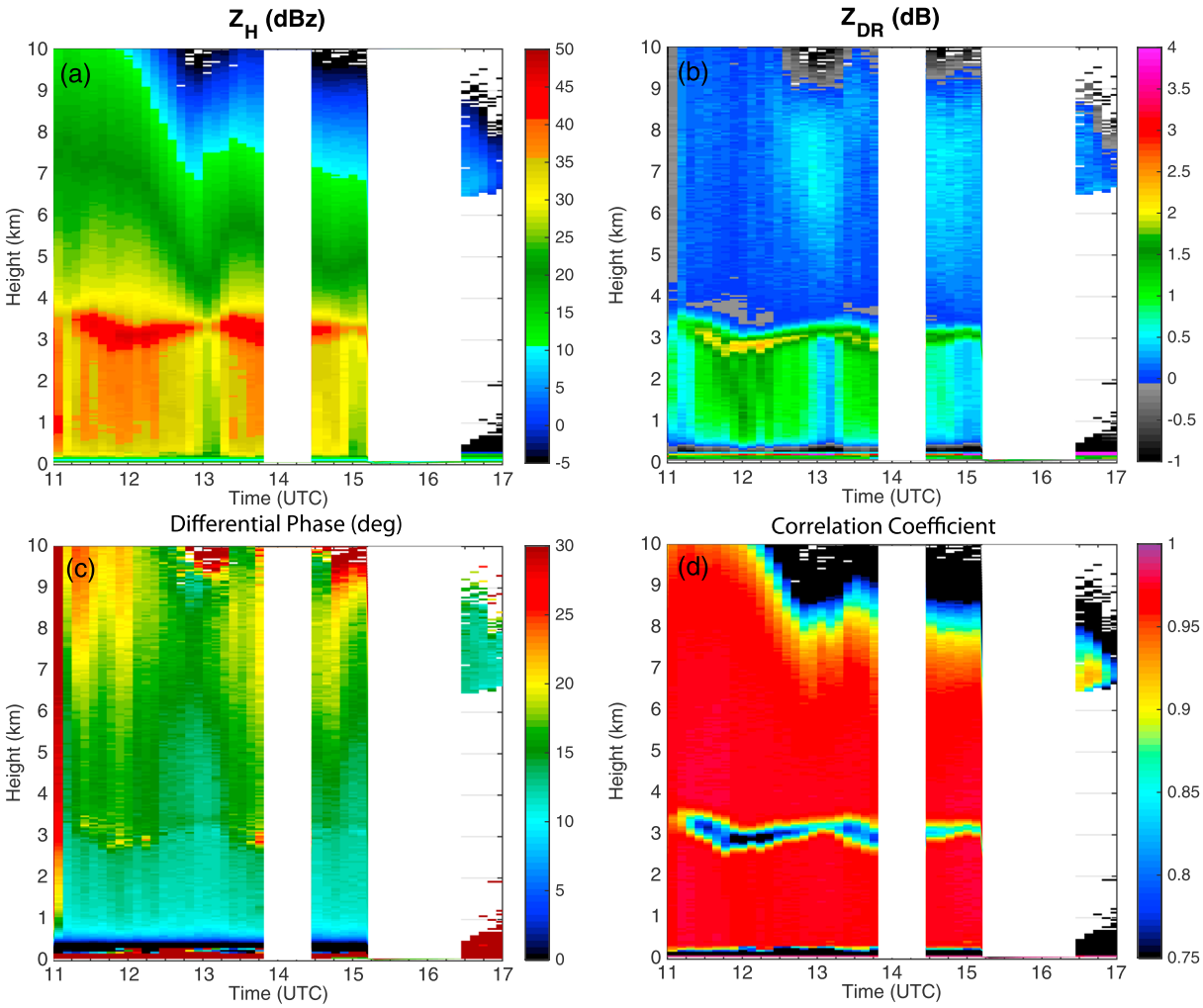

Figure 5. As in Figure 4, but zoomed in to the approximate times of the aircraft measurements. Fields shown are (a) Z_H, (b) Z_{DR}, (c) Φ_{DP}, and (d) ρ_{hv}.

Relative to other times, Z_{DR} values just above the melting layer are consistently reduced by several tenths of a dB during periods of a sagging bright band. This suggests that more isotropic scatterers are present at these times compared to others. Such scatterers may arise owing to decreasing bulk particle density (as in the case of fluffy aggregates), which would tend to drive Z_{DR} toward zero, or to particle shapes becoming less nonspherical, such as may happen in the case of riming or sublimation.

In addition to δ in the melting layer, increases in Φ_{DP} above the melting layer were found in both cases (cf. Figures 3c and 5c). To investigate these enhancements in more detail, we estimate K_{DP} from the Φ_{DP} QVP for both cases (Figure 7). At each time, the averaged Φ_{DP} profile was further smoothed using a 15-gate moving average window. Then, a linear fit within a moving 9-gate window over the smoothed profiles is used to determine K_{DP}. Note that δ in the melting layer was not removed prior to K_{DP} estimation and thus results in a large positive/negative K_{DP} dipole around the melting layer. Between about 0930 and 1030 UTC, the 27 April case features enhanced K_{DP} (>0.2 deg km^{-1}) centered at 3 km agl (Figure 7a), above the sagging melting layer. Air temperatures at this level measured by Citation during this time (Figure 8) are about −4 to −5°C, which favors columnar crystal habits. Average K_{DP} values of 0.2–0.3 deg km^{-1} at C band suggest pristine ice crystal mass contents of roughly 0.3–0.5 g m^{-3}. Such large concentrations of columnar crystals hints at possible secondary ice generation, which is discussed in detail below. Afterward, enhanced K_{DP} exists between 3 and 4 km, corresponding to temperatures between −4 and −10°C. In contrast, the 20 May 2011 case (Figure 7b) only exhibits notable K_{DP} enhancements above about 6 km agl (air temperatures <−12°C) from 1100 to 1300 UTC, favoring planar crystal growth. After this time, maximal K_{DP} values are predominantly above about 5 km agl (temperatures <−5°C).

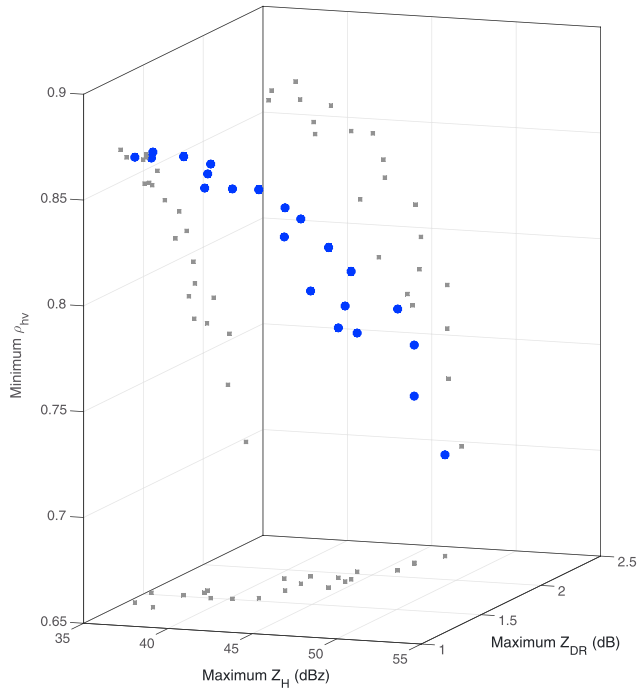

Figure 6. Three-dimensional scatterplot of the maximum Z_H, maximum Z_{DR}, and minimum ρ_{hv} within the 2–4 km agl layer from about 1200 to 1400 UTC on 20 May 2011 (blue circles). The projection of these points onto each two-dimensional plane is shown in gray markers.

Another key piece of information is the observed properties of the bright band itself during these periods of sagging. QVPs of Z_H, Z_{DR}, and ρ_{hv} taken at illustrative times of sagging and no sagging are shown in Figure 9. The radar enhancements follow typical patterns [e.g., *Doviak and Zrnić*, 1993; *Zrnić et al.*, 1993; *Giangrande et al.*, 2008] with the Z_H maximum located above the ρ_{hv} minimum, which is slightly above the Z_{DR} maximum. During bright band sagging, the melting layer deepens and this entire pattern lowers in altitude. In the case of Figure 9, the Z_{DR} enhancement sags by 351 m.

Changes in radar-inferred melting layer top height and/or melting layer depth may arise due to (1) decreased relative humidity, delaying the onset of melting and thereby decreasing the height of the melting layer top; (2) an increased precipitation flux into the melting layer, whereby enhanced cooling leads to an isothermal layer, increasing the depth of the melting layer; (3) changes in vertical air motion, which affect hydrometeor fall speeds and (in the case of downdrafts) tend to promote subsaturated conditions, delaying the onset of melting; or (4) more dense and/or faster-falling particles that fall further before acquiring sufficient meltwater to lead to the Z_{DR} enhancement, decreasing the height of the observed melting layer top.

The first seems unable to explain the observations, given the transient nature of the sagging episodes and the fact that precipitation intensity actually is increased during these times. Snow aggregate fall speeds tend to not increase much with increasing size, not exceeding more than $\sim$ 1m s^{-1} at the ground [e.g., *Locatelli and Hobbs*, 1974; *Brandes et al.*, 2007]. This seems to rule out the possibility of larger, fluffier (less dense) aggregates causing all of the observed features. Larger aggregates would take longer to melt, thereby increasing the melting layer depth and leading to enhanced Z_H within the melting layer. However, the fall speeds of these larger aggregates are similar to those of smaller aggregates, which tends to disfavor the delayed melting (or sagging melting layer enhancements). The second option (increased precipitation flux) would also lead to an increased melting layer depth and enhanced Z_H but would not delay the onset of melting (i.e., would not lead to a sagging of the radar-inferred melting layer top). Large-scale, strong downdrafts ($>$ 1 m s^{-1}) needed to substantially increase fall speeds seem unlikely in quiescent conditions typically found in stratiform precipitation [e.g., *Houze*, 1993].

In contrast, riming could contribute to denser, faster-falling particles that would tend to enhance the Z_H and decrease the Z_{DR} just above the melting layer, all else being equal. Faster-falling rimed particles would tend

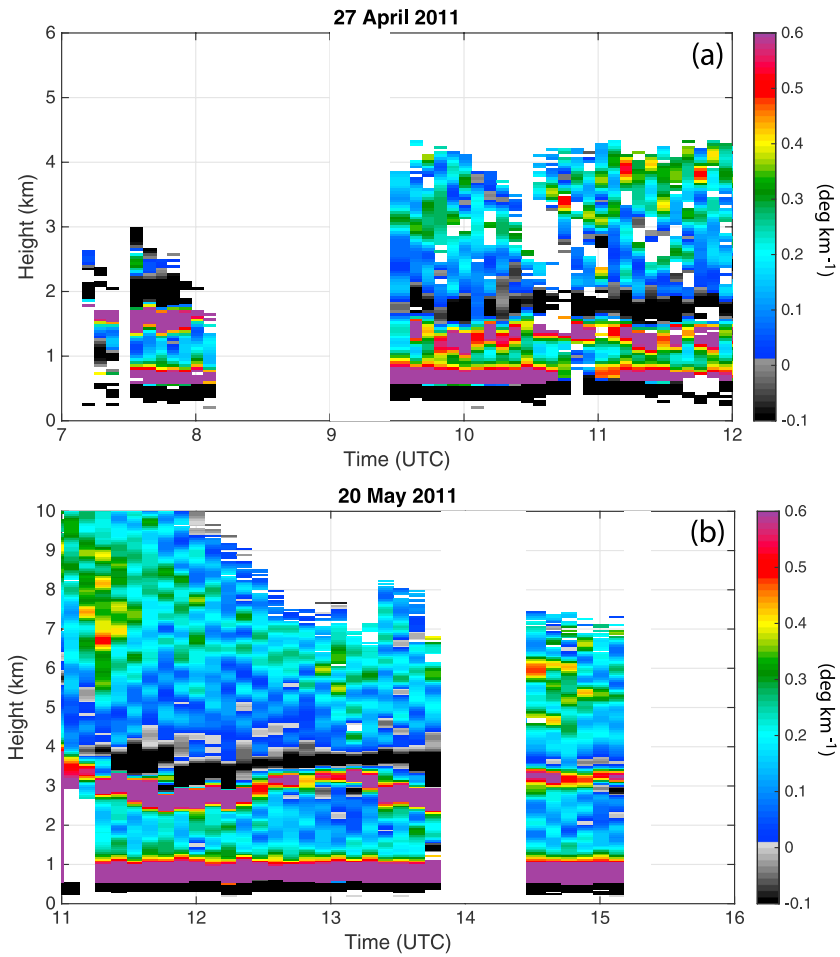

Figure 7. QVPs of the estimated K_{DP} from (a) 27 April 2011 and (b) 20 May 2011. Data are censored where <360° are included in the averaging. K_{DP} is estimated using a 9-gate linear fit to the smoothed Φ_{DP} QVP, which is smoothed using a 15-gate average window. The dipole near the melting layer is associated with backscattering differential phase δ.

to cause a depression in the melting layer height, because particles would descend to lower altitudes before acquiring sufficient meltwater and anisotropy to increase the observed Z_{DR}. Therefore, it is plausible that the saggy bright band signatures are a manifestation of riming. Such faster-falling, denser particles also tend to deepen the melting layer bright band [e.g., *Ryzhkov et al.*, 2008]. Slight deepening of the melting layer was observed in both cases, so any combination of the above processes could also contribute to the observed melting layer deepening.

Both MC3E events exhibit δ within the melting layer at times. Recently, *Trömel et al.* [2014] suggest that large values of δ sometimes observed within the bright band are an indication of large, melting aggregates, whereas smaller values could indicate rimed particles with smaller maximum sizes. Thus, according to the interpretation of *Trömel et al.* [2014], the relatively small (less than about 1°–2°) δ values observed during the saggy bright band events are also consistent with the interpretation of smaller, denser, and/or rimed particles within the melting layer.

Consulting Figure 1a, there is strong evidence for the presence of riming over the ARM site for the 27 April event. There is a pronounced enhancement in the mean Doppler velocity from the RWP, indicating significant ice fall speeds typical only of higher-density rimed particles. Note that in substantial precipitation, backscattering from hydrometeors dominates Bragg scattering [e.g., *Giangrande et al.*, 2013; *Williams*, 2016]. As with the QVP behaviors, the column signatures over the ARM site suggest a sagging in the onset of radar melting signatures (which, in Figure 1a, is a rapid increase in mean Doppler velocity). These are especially evident between about 0900 and 1000 UTC and again between about 1030 and 1100 UTC. Although the signatures

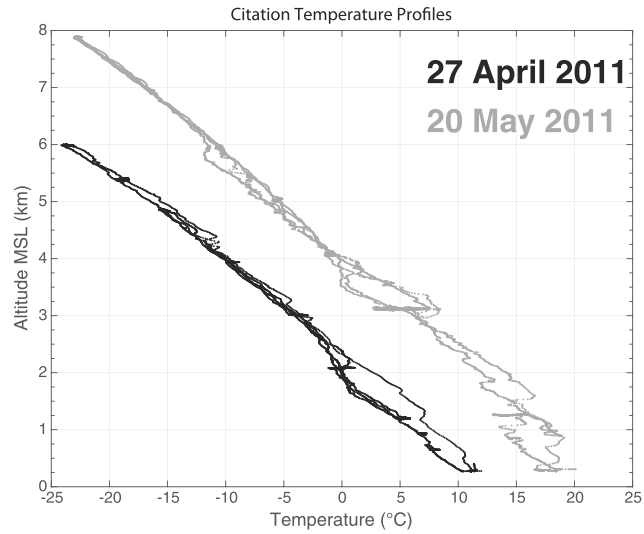

Figure 8. Air temperature as a function of height measured by the UND Citation aircraft throughout its flight for 27 April 2011 (black markers) and 20 May 2011 (gray markers). msl, mean sea level.

of riming are not as prominent over the ARM SGP for the 20 May event, RWP data also indicate the possible presence of higher-density ice over the site at times of bright band sagging. Once again, RWP mean Doppler velocities suggest faster-falling particles above the melting layer for these times (Figure 1b). In addition, one finds similar depressions in melting onset over the site, particularly prior to 1200 UTC and from about 1315 to 1415 UTC. Note that there is no increase in mean Doppler velocity until heights corresponding to temperatures >0°C during the 20 May case, suggesting that particles are in an environment subsaturated with respect to liquid water.

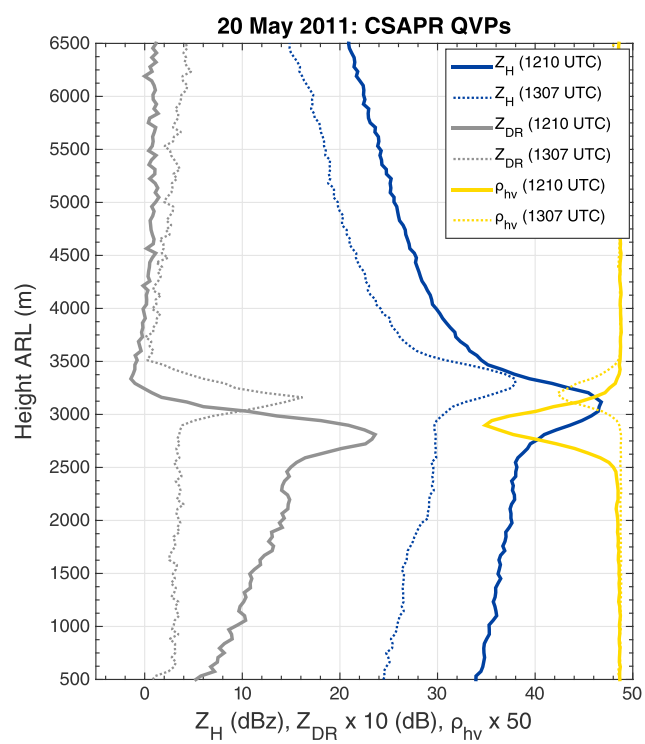

Figure 9. Illustrative QVPs from 20 May 2011 during times with (1210 UTC, solid lines) and without (1307 UTC, dashed lines) bright band sagginess. Profiles show Z_H (blue, in dBZ), Z_{DR} (gray, in dB), and ρ_{hv} (goldenrod). Note that Z_{DR} and ρ_{hv} have been scaled by factors of 10 and 50, respectively, for graphical purposes.

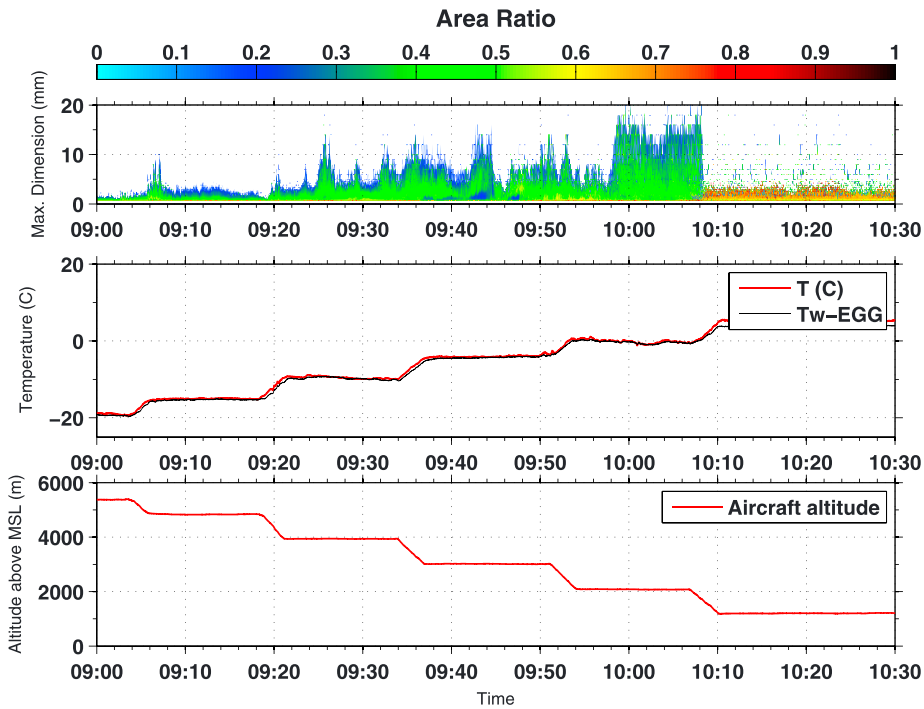

Figure 10. Time series of data from the UND Citation aircraft from 0900 UTC to 1030 UTC on 27 April 2011. (top) The hydrometeor maximum dimension and area ratio calculated by using spectra of the projected area data from HVPS-3 probe; (middle) the air temperature at flight level (*T*, corrected for dynamic heating) and wet-bulb temperature (Tw-EGG), and (bottom) the aircraft altitude.

To complement our radar-based analysis, we next explore microphysical and thermodynamic data from the UND Citation aircraft.

4.4. Aircraft Data

4.4.1. 27 April 2011

The UND Citation aircraft made in situ microphysical and thermodynamic measurements during this event, flying legs, and spirals over the CF, during which its average distance from CSAPR was about 20 km. Figure 10 shows a time series summarizing microphysical and thermodynamic measurements from the UND Citation aircraft over a 1.5 h period leading up to and during the pronounced saggy bright band. Optimally, one should compare times that the Citation aircraft was flying within the conical volume of the CSAPR radar PPIs used for the QVPs. In this way, the aircraft microphysical probe data may be considered representative of the radar signatures.

To do so, the Citation flight track was converted into radar-relative Cartesian coordinates. Times in which the aircraft was within or above the CSAPR beam at a given range are considered within the conical volume. The radar beam height is computed assuming the equivalent $\frac{4}{3}$ Earth radius model for beam propagation [e.g., *Doviak and Zrnić*, 1993]. Unfortunately, the aircraft was not within the conical volume used to create the QVPs during the time of the most pronounced saggy bright band. However, the aircraft was in the 7.8° elevation angle conical volume (Figure 11a) just at the onset of the bright band enhancement and commencement of its sagging, in the period from about 0939 to 0943 UTC. During this time, the aircraft was flying steadily at an altitude of about 3 km msl, with corresponding air temperature near −4°C (Figures 8 and 10).

Interestingly, the probe data reveal a decrease in area ratio (AR) for the smallest particles beginning at about 0937 UTC, along with a reduction in maximum particle dimensions centered at about 0941 UTC. Such small ARs indicate that a particle's projected area is small compared to the area of a circumscribing disk (i.e., circle with the same maximum dimension) [e.g., *Heymsfield and Westbrook*, 2010]. In other words, these small particles are highly nonspherical. The decrease in AR for these small particles suggests the presence of recently nucleated pristine crystals. Indeed, the CIP and 2DC imagery from 0936 to 0947 UTC both reveal a large number of columnar crystals (e.g., Figure 12 shows CIP images from 0943 UTC). Particle images from earlier times (before ~0936 UTC, not shown) when the aircraft was at higher altitudes (and thus lower temperatures)

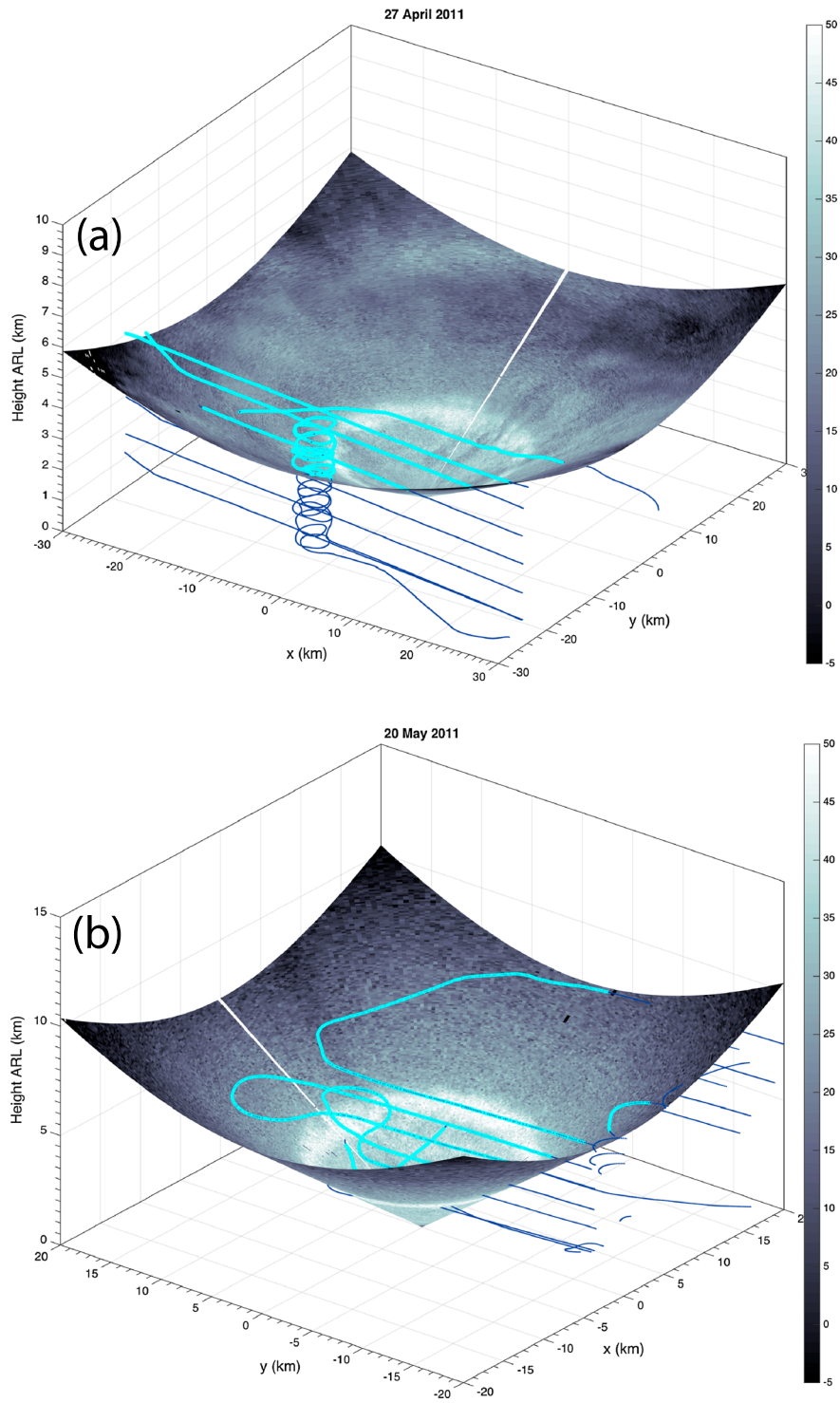

Figure 11. Three-dimensional representation of the CSAPR conical scan surface showing Z_H (dBz, shaded according to scale) overlaid with the Citation aircraft track for (a) 7.8° PPI from 27 April 2011 at 1000 UTC and (b) 21.4° PPI from 20 May 2011 at 1345 UTC. The aircraft track is highlighted in cyan when the Citation was within the conical scan volume.

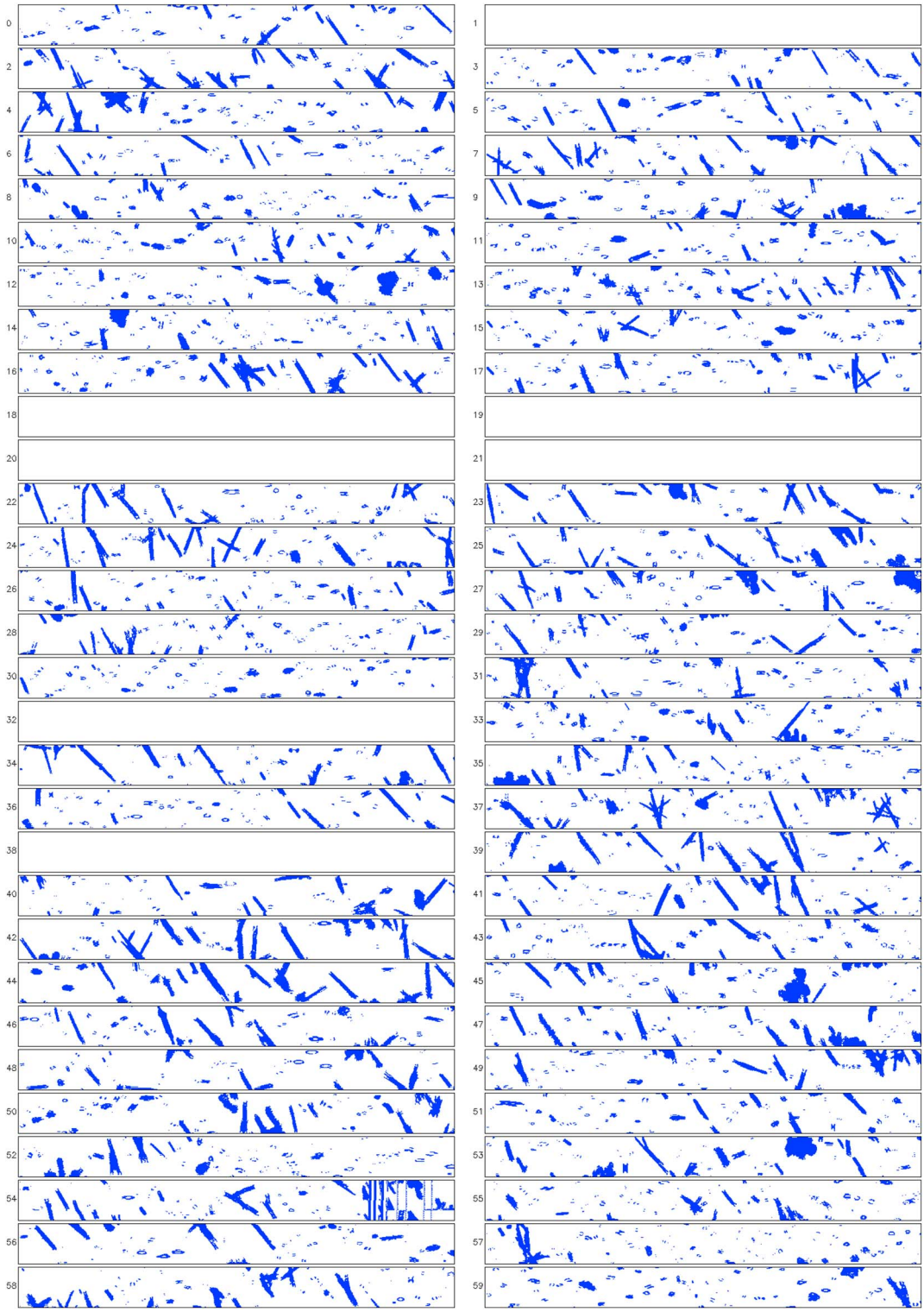

Figure 12. CIP images of hydrometeor shadows for a 1 min period starting at 0943 UTC on 27 April 2011. Each panel corresponds to a second. The height of each panel represents 1.6 mm.

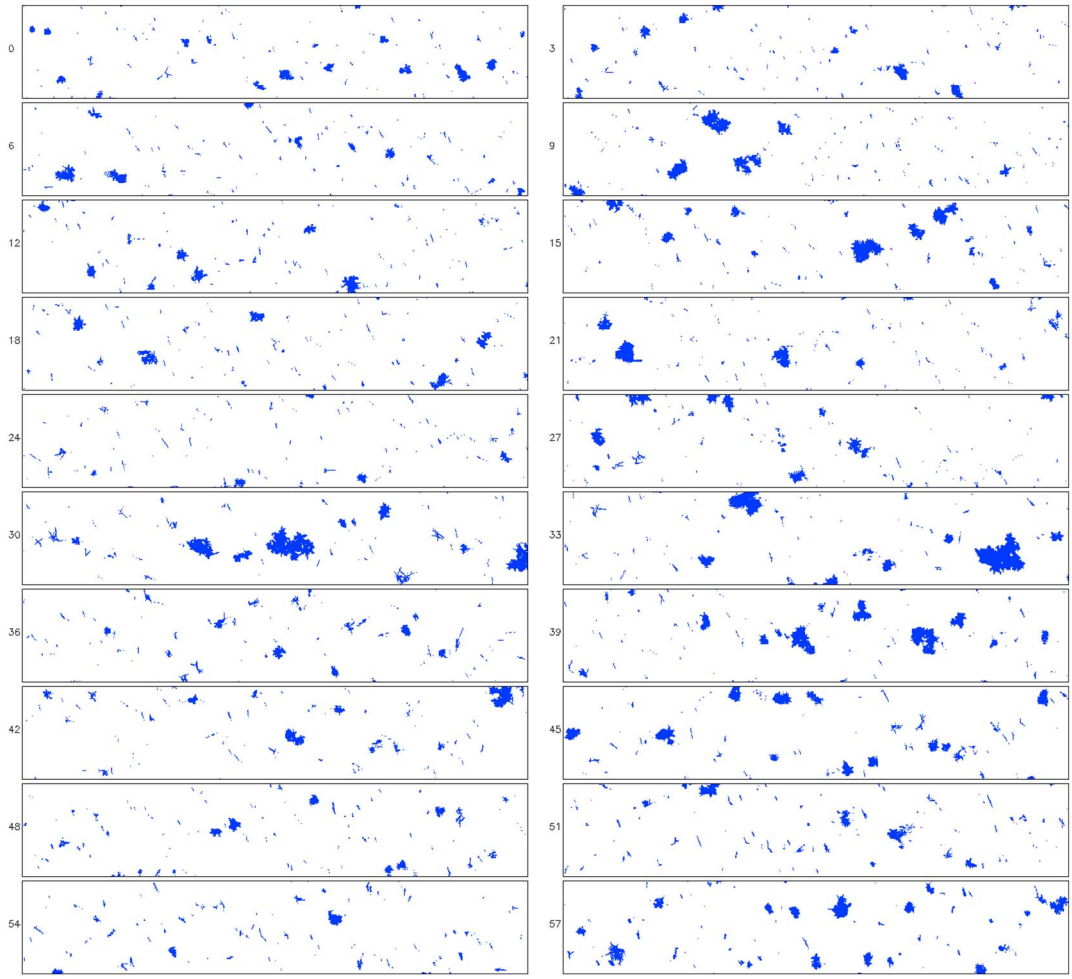

Figure 13. HVPS-3 images of hydrometeor shadows for a 1 min period starting at 0943 UTC on 27 April 2011. Each panel corresponds to 3 s. The height of each panel represents 19.2 mm.

did not have appreciable numbers of columns/needles, suggesting that the needles did not sediment from aloft. The aircraft descended between 0951 and 0954 UTC and entered the melting layer, and the needles were no longer visible. Thus, the data suggest that the needles were generated locally. The small needle-like crystals could explain the AR reduction at small sizes discussed above. In addition to the needles, HVPS-3 imagery (Figure 13) also reveals the presence of some larger aggregates as well as smaller, possibly rimed particles.

The liquid water content measured from the King probe and cloud droplet total number concentration measured from the CDP (Figure 14) both increase sharply shortly after 0944 UTC, with relative humidity values implying saturation with respect to liquid water (and thus supersaturation with respect to ice). The Rosemount icing sensor detected supercooled liquid water between 0947 and 0951 UTC (not shown). Though not within the CSAPR conical volume, the flight is at the same altitude (and temperature) throughout the period (0944–0951 UTC). This suggests that the aircraft is encountering updrafts capable of producing supercooled liquid water droplets. Vertical velocity estimates from the aircraft data indicate upward motion at this time as well, with 5 s average values occasionally exceeding 0.5 m s^{-1} between 0944 and 0946 UTC (not shown). Five second averaged downward air velocities rarely exceed 0.5 m s^{-1} in magnitude, consistent with *Houze* [1993] and suggesting that widespread downdrafts are not a major contributor to bright band sagging. Total water content values during the time of observed needles (0.3–0.4 g m^{-3}) are consistent with the K_{DP}-based ice water content estimate from CSAPR discussed above. The presence of a large number of needles in the immediate vicinity of this rising motion, temperatures of about −4°C, and enhanced liquid water contents plausibly could be the result of secondary ice production (e.g., rime splintering via the Hallett-Mossop mechanism). The high temperatures discount the possibility of primary ice nucleation.

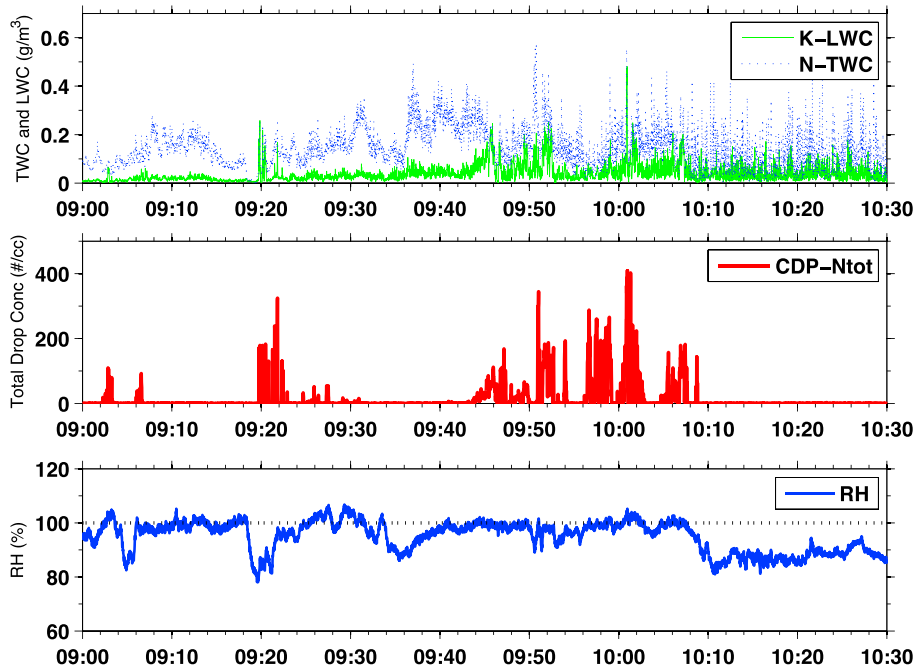

Figure 14. Time series of probe measurements from the UND Citation aircraft from 0900 to 1030 UTC on 27 April 2011. (top) Liquid water content from the King probe (green) and total water content from the Nevzorov probe (blue dotted) in g m^{-3}; (middle) total liquid drop number concentration (cm^{-3}) from the Cloud Droplet Probe (CDP; particles <10 μm are not included in the total concentration); (bottom) relative humidity (%) with respect to liquid water.

Therefore, we argue that the evidence from the aircraft data supports ongoing riming, consistent with the inferences made from the CSAPR observations of the saggy bright band signature.

After 0953 UTC, the aircraft is in the melting layer (see Figure 10); spikes in CDP-derived total number concentration after this point could be a manifestation of particle melting. Starting at about 0958 UTC, there is a sudden increase in the concentration of large (maximum dimension >10 mm) particles. These large particles are thought to arise from aggregation within the melting layer.

4.4.2. 20 May 2011

The Citation aircraft also was used for in situ measurements during the 20 May 2011 case. The time series of the AR size distribution, air temperature, and altitude of the Citation aircraft during a time period of interest on 20 May 2011 are shown in Figure 15. The aircraft was within the 21.4° elevation angle conical volume averaged for the QVP (Figure 11b) from about 1337 to 1346 UTC, at a time when the saggy bright band was evident (cf. Figure 5). At the beginning of this period, the Citation ascended from near −0.5°C to about −6°C, where it remained for several minutes (Figure 15). Unlike the 27 April case, we do not see ARs indicative of highly nonspherical small crystals (sizes ~1 mm). Instead, AR values suggest the presence of a mixture of large aggregates (AR ~ 0.2) and relatively smaller, more spherical particles (AR ~0.5). AR values of about 0.5 in the size range from 1 mm to 10 mm could be an indication of the presence of rimed quasi-spherical crystals, or other compact, isometric particles.

Also, in contrast to 27 April 2011, the aircraft-measured relative humidity with respect to liquid water is well below 100% throughout much of the period (Figure 16). Liquid water content and cloud droplet number concentration are also minimal, whereas ice water content is large. Thus, conditions at the aircraft flight level during this period are not favorable for ongoing riming. In fact, the low relative humidity values with respect to liquid water (~90%) measured at flight level ($T \approx -6$°C) indicate that conditions are subsaturated with respect to ice, suggesting that sublimation likely was occurring at flight level.

CIP images from this period reveal the presence of a few aggregates and numerous small, roundish hydrometeors (Figure 17). These smaller hydrometeors have no discernable crystalline structure, but relatively simple outlines. This suggests that they are not pristine crystals, but rather compact, more isometric, denser particles. The lack of pristine ice is consistent with the lack of enhanced K_{DP} values observed with CSAPR at these temperatures. HVPS-3 images also starkly contrast the 27 April 2011 case (Figure 18), revealing a lack of

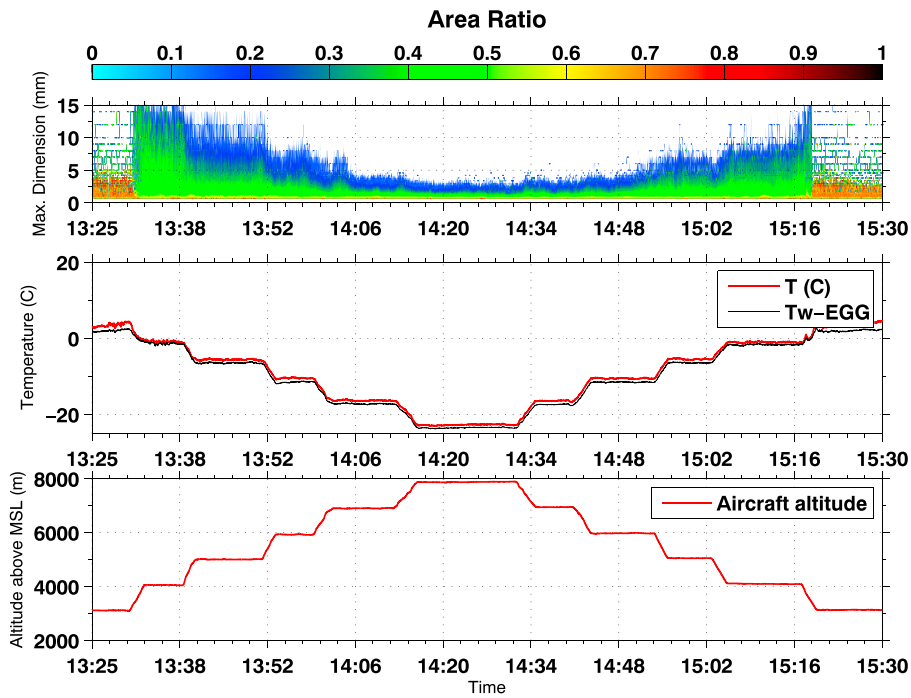

Figure 15. As in Figure 10, but from 1325 UTC to 1530 UTC on 20 May 2011.

large aggregates, and instead featuring a number of smaller, compact, roundish hydrometeors. Though rimed particles may appear this way in particle images, the aircraft thermodynamic data argue strongly against riming at this level. Instead, small aggregates undergoing sublimation would take on more rounded appearances as the branches/tips of constituent crystals are preferentially depleted [e.g., *Sulia and Harrington*, 2011]. Thus, unless riming occurred recently and/or at a different altitude than the flight level, the aircraft data suggest that sublimation may have produced more compact particles that contributed to the saggy bright band signature in this case.

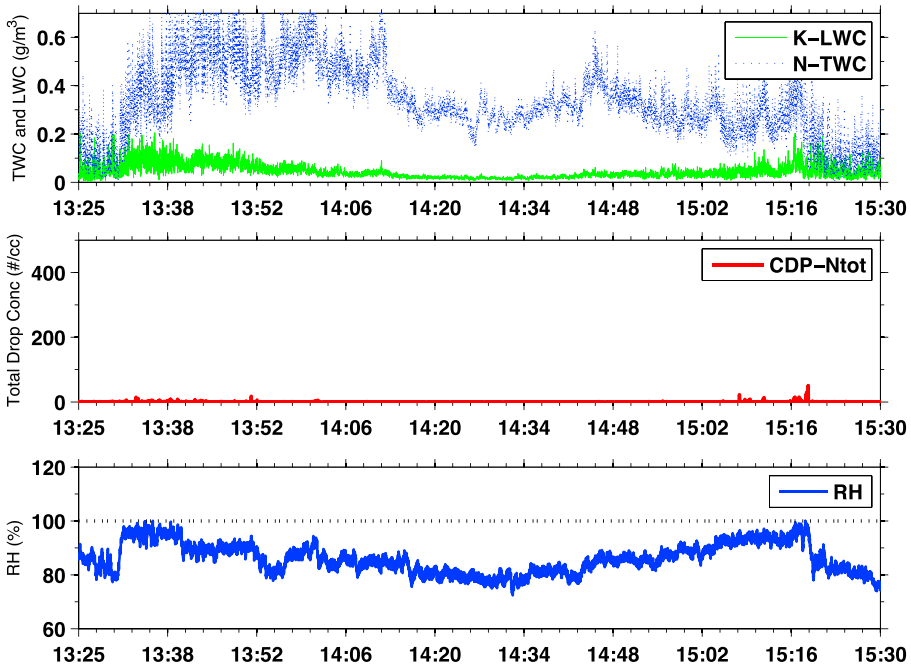

Figure 16. As in Figure 14, but from 1325 UTC to 1530 UTC on 20 May 2011.

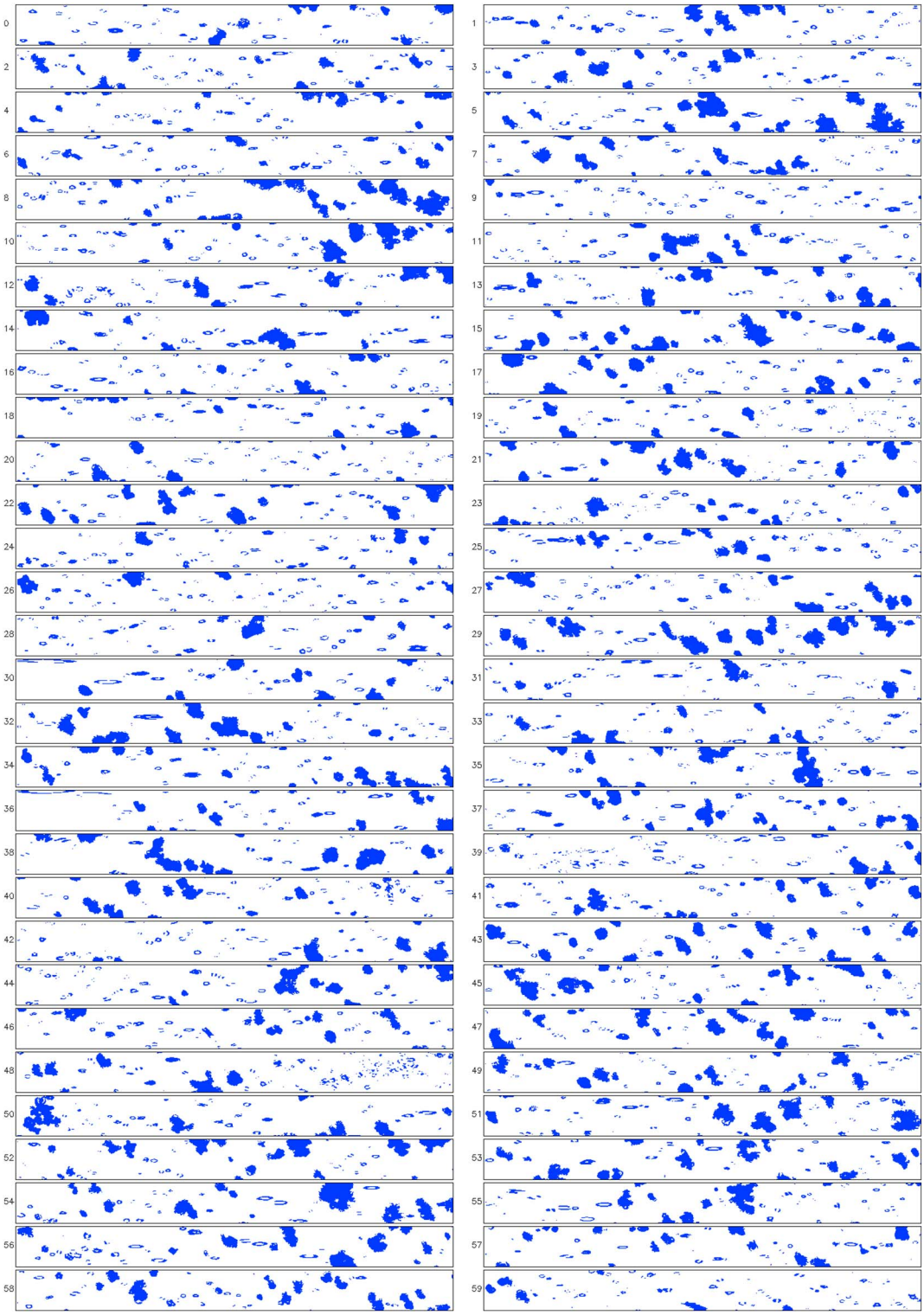

Figure 17. CIP images of hydrometeor shadows for a 1 min period starting at 1345 UTC on 20 May 2011. Each panel corresponds to a second. The height of each panel represents 1.6 mm.

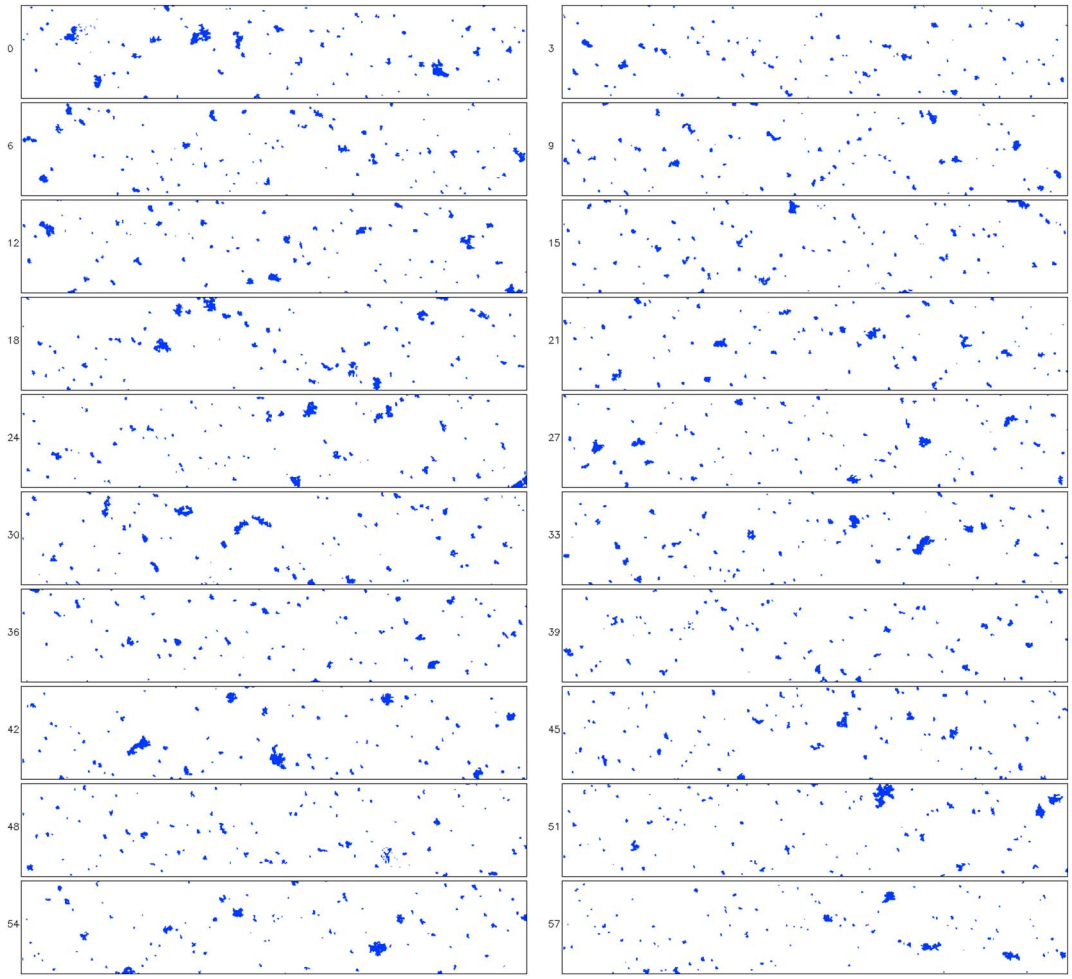

Figure 18. HVPS-3 images of hydrometeor shadows for a 1 min period starting at 1345 UTC on 20 May 2011. Each panel corresponds to 3 s. The height of each panel represents 19.2 mm.

5. Microphysical Model Simulations

A simple one-dimensional bin microphysical model of melting aggregates is used to explore the plausibility of denser, faster-falling particles as an explanation for the saggy bright band observations discussed above. The model is similar to the ones used by *Giangrande* [2007], *Trömel et al.* [2013], *Trömel et al.* [2014], and *Ryzhkov et al.* [2014a]; the reader is referred to those studies for more details. At the top of the domain, an initial distribution of dry aggregates is prescribed as 80 independent size bins. Note that although needles were observed in the 27 April case, we do not consider pristine crystals in this model as they are not expected to contribute significantly to the overall Z_H. These aggregates then descend through an environment based on prescribed vertical profiles of temperature, relative humidity, and pressure. The model tracks mass water fraction and density of snowflakes in each size bin as they melt. Melting follows standard heat balance equations [e.g., *Szyrmer and Zawadzki*, 1999; *Zawadzki et al.*, 2005; *Ryzhkov et al.*, 2013a] for individual size bins; interactions among different size bins (e.g., collisions, aggregation, and coalescence) are not taken into account. The snow particle size distributions aloft are initialized such that after complete melting, they produce a distribution of raindrops at the surface equal to the median drop size distribution for a given Z_H observed in a large 2-D video disdrometer data set from Oklahoma [*Schuur et al.*, 2005]. In other words, the snow size distributions aloft are determined assuming the conservation of particle flux through the transition from snow to rain [e.g., *Zhang et al.*, 2011] by prescribing a Z_H for rain at the surface.

To emulate the appearance of denser, faster-falling particles, the snowflake distributions are modified by assuming different degrees of riming on the aggregates aloft ($f_{\mathrm{rime}} = 1$ for unrimed snow, $f_{\mathrm{rime}} = 5$ for

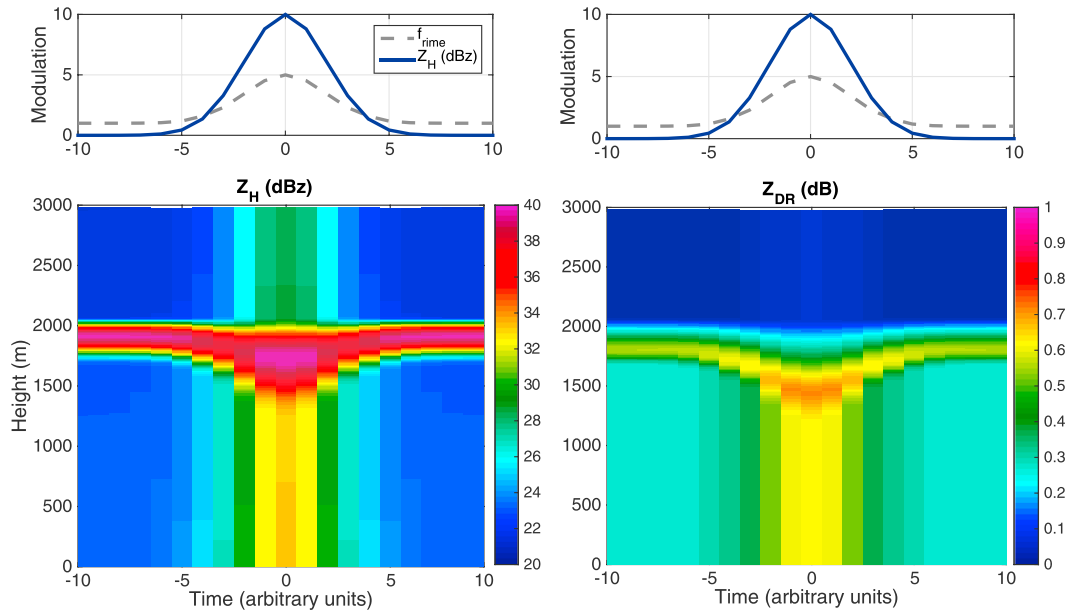

Figure 19. Microphysical model simulations of time-height profiles of (left column) Z_H and (right column) Z_{DR}. (top row) The degree of riming (f_{rime}) on snow crystals above the melting layer follows a Gaussian function centered on time $t = 0$ with a maximum of 5 and minima of 1 (gray curves). The particle size distributions are also modulated such that the nominal rain reflectivity factor varies as a Gaussian function centered on time $t = 0$, with minima of 25 dBz and a maximum of 35 dBz (Figure 19, top row, blue curves).

heavily rimed snow). The density of snowflakes aloft decreases with increasing particle size and increases within increasing f_{rime}, following *Brandes et al.* [2007] and *Zawadzki et al.* [2005]:

$$\rho_{snow}(D) = 0.178 f_{rime} D^{-0.922}. \tag{1}$$

In equation (1), D is in mm, and ρ_{snow} is in g cm^{-3}. Snow fall speeds increase with f_{rime}, following *Zawadzki et al.* [2005]. In this way, "riming" produces denser, faster-falling snowflakes. The microphysical model output is converted to the polarimetric radar variables following *Ryzhkov et al.* [2011].

To simulate a local enhancement of riming above the melting layer, f_{rime} is modulated as a Gaussian function from its minimum value $f_{rime} = 1$ at arbitrary times $t = -10$ and $t = 10$ to its maximum value ($f_{rime} = 5$) at an arbitrary time $t = 0$. Previous studies using this approach [e.g., *Zawadzki et al.*, 2005; *Ryzhkov et al.*, 2008] fix Z_H in the rain and vary f_{rime} aloft. As a result, mass spectra aloft are identical, whereas the size distributions vary with f_{rime}. Thus, melting layer characteristics are compared for a population of larger, fluffy aggregates versus smaller, denser, rimed aggregates that produce the same rain Z_H. In this approach, the bright band enhancements in all radar variables are reduced with increasing f_{rime}. In contrast, the MC3E cases feature enhanced Z_H aloft and in rain at times of sagging, suggesting wider ice mass spectra aloft. Thus, to capture this increased mass flux, the nominal rain Z_H for the PSDs is modulated from a minimum of 25 dBz at times $t = -10$ and $t = 10$ to a maximum of 35 dBz at $t = 0$ (Figure 19, top row). Note that we do not change the axis ratio of the particles as we increase the rime fraction. In real clouds, it may be expected that initially oblate pristine particles become less nonspherical owing to riming [e.g., *Mosimann et al.*, 1994; *Ryzhkov et al.*, 2014b; *Jensen and Harrington*, 2015]. Scattering calculations by *Vogel et al.* [2015] confirm such Z_{DR} reductions with increased riming.

The simulated time-height profiles of Z_H and Z_{DR} are shown in Figure 19. The melting layer bright band is enhanced at time $t = 0$, with larger Z_H values extending lower than at earlier and later times. Similarly, the Z_{DR} profile shows enhanced values at the bottom of the melting layer centered on time $t = 0$. Additionally, the Z_{DR} profile shows a clear "sagging" of the bright band top and bottom by a few hundred meters. This behavior is strikingly similar to the observed saggy bright band signatures in the CSAPR QVPs (cf. Figure 9). The enhanced density and fall speeds of the rimed snow particles allows them to descend further before complete melting. Sensitivity tests (not shown) indicate that the degree of riming (f_{rime}) modulation and its associated effects on particle fall speeds and densities is the most important factor in reproducing the saggy

bright band. For example, in the simulation shown in Figure 19, the height of the maximum Z_{DR} value sags a maximum of 360 m. A sensitivity run in which there is no Gaussian modulation of f_{rime} but in which there is a modulation of the nominal rain Z_H results in a maximum Z_{DR} sagging of only 90 m. In contrast, a sensitivity run with the f_{rime} modulation but no modulation of the nominal rain Z_H results in a sagging of 210 m. Thus, these simplified simulations suggest that the majority of bright band sagging results from the modulation of riming degree f_{rime} and associated increases in particle densities and fall speeds, with a secondary contribution from increased precipitation rate.

No thermodynamic feedbacks were considered in these simple simulations. One may expect an increased precipitation flux into the melting layer to increase the local cooling as melting particles extract thermal energy from the environment, thereby deepening the melting layer [e.g., *Kain et al.*, 2000]. Thus, inclusion of these effects could increase the precipitation rate contribution to melting layer depth. However, this effect will not significantly decrease the height at which melting begins (i.e., will not contribute to Z_{DR} sagging). Additionally, an enhanced precipitation flux into the melting layer does not explain the reduction of Z_{DR} found just above the saggy bright band. Recent observations of snow aggregates in convective storm anvils by *Homeyer and Kumjian* [2015] suggest that Z_{DR} is nearly constant (or slightly increases) with increasing Z_H. This is inconsistent with the QVP observations, which instead show a tendency for *more isotropic* scattering particles above the saggy bright bands.

6. Discussion and Conclusions

Quasi-vertical profiles (QVPs) of the polarimetric radar variables in regions of stratiform precipitation during two MC3E storms revealed transient, subtle changes in the melting layer bright band structure. Such subtle signatures are very difficult to observe in traditional PPI scans but are quite clear in the azimuthally averaged QVP time-height plots. In particular, a clear sagging of the bright band enhancement in Z_{DR} and ρ_{hv} is observed, with noticeably reduced Z_{DR} present just above the sagging signature. Recent scanning S band radar and vertically pointing X band radar observations presented in *Vogel et al.* [2015] suggest that such Z_{DR} reductions can occur during heavy riming periods. This saggy bright band signature is interpreted as the addition of denser, faster-falling particles falling into the melting layer. These more isotropically scattering particles cause a Z_{DR} reduction and Z_H enhancement above the melting layer. Their increased fall speeds allow them to descend greater distances before accumulating sufficient meltwater to enhance the Z_{DR}, leading to the local sagging of the bright band and an increase in its depth. Vertically pointing mean Doppler velocity observations from the SGP site RWP confirm the presence of faster-falling particles above the melting layer in both cases. In one case (27 April 2011), CSAPR QVPs show enhanced K_{DP} values just above the saggy bright band, at temperatures of −4 to −5°C. This suggests high concentrations of pristine columnar or needle-like crystals which could be generated by secondary ice production.

Limited in situ data are available for these cases from the University of North Dakota Citation aircraft. In the 27 April 2011 case, numerous needles were indeed observed coincident with the onset of bright band sagging, confirming the inferences from the CSAPR K_{DP} observations. These needles were not observed at other levels and produced a distinct decrease in the area ratio of smaller hydrometeors. Given the appearance of the needles and their context within an environment supportive of secondary ice production via riming, we suggest that they provide circumstantial evidence that riming was occurring. Collocated aircraft measurements of upward vertical velocities and liquid droplets support these conclusions. Further, additional observations from the ARM profiling radar and in the companion aircraft spiral analysis (S. E. Giangrande et al., submitted manuscript, 2016). demonstrate that pockets of riming were present at other times during this event.

In contrast, little evidence of riming at aircraft flight level is found on 20 May. Instead, thermodynamic data suggest conditions favoring sublimation, which could lead to more compact, isotropically scattering particles. Citation aircraft data from the 20 May 2011 case did not reveal needles but did exhibit a large number of small, round hydrometeors at −6°C that are interpreted to be dense aggregates undergoing sublimation. Together, limited in situ data from these two cases provide evidence that along with aggregates, denser particles were present at times when the CSAPR QVPs revealed saggy bright bands.

A simple, one-dimensional bin microphysical model of melting snow with varying degrees of riming was used to reproduce the saggy bright band signature in an effort to test the radar data interpretation and the signature's microphysical origin. The simulated Z_H and Z_{DR} fields agree surprisingly well with the observed

QVP signatures. Sensitivity tests indicated that modulation of riming degree, which increases particle density and fall speed, was the most important factor leading to a reduction in the top of the Z_{DR} bright band enhancement height. Increased unrimed snowfall rate above the melting layer, though not negligible, was of secondary importance. The modeling results strongly suggest that riming of snowflakes falling into the melting layer can produce signatures strikingly similar to the observed saggy bright bands. By analogy, other mechanisms leading to dense, fast-falling particles can also produce bright band sagging. Widened mass spectra aloft can account for enhancements in all radar variables within the melting layer.

The saggy bright band occurred several times during the two MC3E cases. Analyzing more cases from different radars and in different environmental contexts could reveal additional insights into the repeatability of this signature. Such subtle signatures likely are observable only when averaging is performed (e.g., QVPs) given the noisiness of data often found in traditional PPI or RHI scans. If found to be reliable, we suggest that such QVP analyses may be an effective way to monitor the melting layer bright band for changes associated with different microphysical processes. Such a clear distinction between the signatures in the QVP analyses is possible because of the reduced statistical errors in estimates of the radar variables compared to conventional PPI or RHI scans. Monitoring of the bright band with QVPs could provide information about changes in the microphysical characteristics of hydrometeors above and within the melting layer, which may affect the accuracy of quantitative precipitation estimates.

Ultimately, additional in situ data collected within the radar conical volume and coincident with the radar scans could help determine the reliability of saggy bright bands as an indicator of riming versus other factors (e.g., sublimation). Such data could facilitate developing a quantitative relationship between the radar signatures and the degree of riming and/or liquid water content. This type of relationship could allow saggy bright band observations to imply the presence (and possible amount) of supercooled liquid water aloft, which may provide important information in mitigating aircraft icing risks and be a helpful constraint for microphysical modeling studies.

Acknowledgments
Support for this work comes from grant ER65459 from the U.S. Department of Energy Atmospheric System Research program. Support for A. Ryzhkov and S. Mishra comes from NOAA/Office and Atmospheric Research under NOAA-University of Oklahoma cooperative agreement NA11OAR4320072, U.S. Department of Commerce. Support for A. Bansemer is from DOE ASR grant DE-SC0008648. We would like to thank Mike Poellet and his research group at UND for processing and providing the in situ aircraft data. Radar data are available at the Department of Energy Atmospheric Radiation Measurement program data archive. We would also like to thank Sandra Yuter (NCSU) for helpful criticisms of our work. The comments and suggestions from three anonymous reviewers significantly improved the clarity and presentation of the manuscript. The National Center for Atmospheric Research is sponsored by the National Science Foundation.

References

Andrić, J., M. R. Kumjian, D. S. Zrnić, J. M. Straka, and V. M. Melnikov (2013), Polarimetric signatures above the melting layer in winter storms: An observational and modeling study, *J. Appl. Meteorol. Climatol.*, *52*, 682–700.

Bailey, M. P., and J. Hallett (2009), A comprehensive habit diagram for atmospheric ice crystals: Confirmation from the laboratory, AIRS II, and other field studies, *J. Atmos. Sci.*, *66*, 2888–2899.

Bechini, R., L. Baldini, and V. Chandrasekar (2013), Polarimetric radar observations of the ice region of precipitation clouds at C-band and X-band radar frequencies, *J. Appl. Meteorol. Climatol.*, *52*, 1147–1169.

Black, M. L., R. W. Burpee, and F. D. Marks (1991), Vertical motions in tropical cyclones determined with airborne Doppler radial velocities, in *19th Conference on Hurricanes and Tropical Meteorology*, pp. 409–411, AMS, Preprints, Miami, Fla.

Black, M. L., R. W. Burpee, and F. D. Marks (1996), Vertical motion characteristics of tropical cyclones determined with airborne Doppler radial velocities, *J. Atmos. Sci.*, *53*, 1887–1909.

Brandes, E. A., K. Ikeda, G. Zhang, M. Schönhuber, and R. Rasmussen (2007), A statistical and physical description of hydrometeor distributions in Colorado snowstorms using a video-disdrometer, *J. Appl. Meteorol.*, *46*, 634–650.

Bringi, V. N., and V. Chandrasekar (2001), *Polarimetric Doppler Weather Radar*, 1st ed., 636 pp., Cambridge Univ. Press, Cambridge, U. K.

Cober, S. G., G. A. Isaac, and A. V. Korolev (2001), Assessing the Rosemount icing detector with in situ measurements, *J. Atmos. Oceanic Technol.*, *18*, 515–528.

Doviak, R. J., and D. S. Zrnić (1993), *Doppler Radar and Weather Observations*, 2d ed., 562 pp., Academic Press, San Diego, Calif.

Fabry, F., G. L. Austin, and D. Tees (1992), The accuracy of rainfall estimates by radar as a function of range, *Q. J. R. Meteorol. Soc.*, *118*, 435–453.

Giangrande, S. E. (2007), Investigation of polarimetric measurements of rainfall at close and distant ranges, PhD dissertation, Univ. of Okla.

Giangrande, S. E., S. Collis, J. Straka, A. Protat, C. Williams, and S. Krueger (2013), A summary of convective-core vertical velocity properties using ARM UHF wind profilers in Oklahoma, *J. Appl. Meteorol. Climatol.*, *52*, 2278–2295.

Giangrande, S. E., S. Collis, A. K. Theisen, and A. Tokay (2014), Precipitation estimation from the ARM distributed radar network during the MC3E campaign, *J. Appl. Meteorol. Climatol.*, *53*, 2130–2147.

Giangrande, S. E., J. M. Krause, and A. V. Ryzhkov (2008), Automated designation of the melting layer with a polarimetric prototype of the WSR-88D radar, *J. Appl. Meteorol. Climatol.*, *47*, 1354–1364.

Herzegh, P. H., and A. R. Jameson (1992), Observing precipitation through dual-polarization radar measurements, *Bull. Am. Meteorol. Soc.*, *73*, 1365–1374.

Heymsfield, A. J., and C. D. Westbrook (2010), Advances in the estimation of ice particle fall speeds using laboratory field measurements, *J. Atmos. Sci.*, *67*, 2469–2482.

Hogan, R., P. Field, A. Illingworth, R. Cotton, and T. Choularton (2002), Properties of embedded convection in warm-frontal mixed-phase cloud from aircraft and polarimetric radar, *Q. J. R. Meteorol. Soc.*, *128*, 451–476.

Homeyer, C. R., and M. R. Kumjian (2015), Microphysical characteristics of overshooting convection from polarimetric radar observations, *J. Atmos. Sci.*, *72*, 870–891.

Hou, A. Y., et al. (2014), The Global Precipitation Measurement mission, *Bull. Am. Meteorol. Soc.*, *95*, 701–722.

Houze, R. A. (1993), *Cloud Dynamics*, 1st ed., 573 pp., Academic Press, Oxford, U. K.

Jensen, A. A., and J. Y. Harrington (2015), Modeling ice crystal aspect ratio evolution during riming: A single particle growth model, *J. Atmos. Sci.*, *72*, 2569–2590.

Jensen, M., et al. (2016), The Midlatitude Continental Convective Clouds Experiment (MC3E), *Bull. Am. Meteorol. Soc.*, doi:10.1175/BAM-S-D-14-00228.1.

Kain, J. S., S. M. Goss, and M. E. Baldwin (2000), The melting effect as a factor in precipitation-type forecasting, *Weather Forecasting*, *15*, 700–714.

Kennedy, P. C., and S. A. Rutledge (2011), S-band dual-polarization radar observations of winter storms, *J. Appl. Meteorol. Climatol.*, *50*, 844–858.

Knollenberg, R. G. (1981), Techniques for probing cloud microstructure, in *Clouds, Their Formation, Optical Properties, and Effects*, pp. 15–91, Academic Press, New York.

Kumjian, M. R. (2013a), Principles and applications of dual-polarization weather radar. Part I: Description of the polarimetric radar variables, *J. Oper. Meteorol.*, *1*, 226–242.

Kumjian, M. R. (2013b), Principles and applications of dual-polarization weather radar. Part II: Warm and cold season applications, *J. Oper. Meteorol.*, *1*, 243–264.

Kumjian, M. R. (2013c), Principles and applications of dual-polarization weather radar. Part III: Artifacts, *J. Oper. Meteorol.*, *1*, 265–274.

Kumjian, M. R., S. A. Rutledge, R. M. Rasmussen, P. C. Kennedy, and M. Dixon (2014), High-resolution polarimetric radar observations of snow-generating cells, *J. Appl. Meteorol. Climatol.*, *53*, 1636–1658.

Kumjian, M. R., A. V. Ryzhkov, H. D. Reeves, and T. J. Schuur (2013), A dual-polarization radar signature of hydrometeor refreezing in winter storms, *J. Appl. Meteorol. Climatol.*, *52*, 2549–2566.

Kumjian, M. R., and A. D. Schenkman (2014), The curious case of ice pellets in Middle Tennessee on 1 March 2014, *J. Oper. Meteorol.*, *2*(17), 209–213.

Lamb, D., and J. Verlinde (2011), *Physics and Chemistry of Clouds*, 1st ed., 600 pp., Cambridge Univ. Press, Cambridge, U. K.

Lawson, R. P., R. E. Stewart, and L. J. Angus (1998), Observations and numerical simulations of the origin and development of very large snowflakes, *J. Atmos. Sci.*, *55*, 3209–3229.

Locatelli, J. D., and P. V. Hobbs (1974), Fall speeds and masses of solid precipitation particles, *J. Geophys. Res.*, *79*, 2185–2197.

Mather, J. H., and J. W. Voyles (2013), The ARM Climate Research Facility: A review of structure and capabilities, *Bull. Am. Meteorol. Soc.*, *94*, 377–392.

Mittermaier, M. P., R. J. Hogan, and A. J. Illingworth (2004), Using mesoscale model winds for correcting wind-drift errors in radar estimates of surface rainfall, *Q. J. R. Meteorol. Soc.*, *130*, 2105–2123.

Morrison, H., and J. A. Milbrandt (2015), Parameterization of microphysics based on the prediction of bulk ice particle properties. Part I: Scheme description and idealized tests, *J. Atmos. Sci.*, *72*, 287–311.

Morrison, H., J. A. Milbrandt, G. H. Bryan, K. Ikeda, S. A. Tessendorf, and G. Thompson (2015), Parameterization of cloud microphysics based on the prediction of bulk ice particle properties. Part II: Case study comparisons with observations and other schemes, *J. Atmos. Sci.*, *72*, 312–339.

Mosimann, L., E. Weingartner, and A. Waldvogel (1994), An analysis of accreted drop sizes and mass of rimed snow crystals, *J. Atmos. Sci.*, *51*, 1548–1558.

Oue, M., M. R. Kumjian, Y. Lu, Z. Jiang, E. E. Clothiaux, J. Verlinde, and K. Aydin (2015a), X-band polarimetric and Ka-band Doppler spectral radar observations of a graupel-producing Arctic mixed-phase cloud, *J. Appl. Meteorol. Climatol.*, *54*, 1335–1351.

Oue, M., M. R. Kumjian, Y. Lu, J. Verlinde, K. Aydin, and E. E. Clothiaux (2015b), Linear depolarization ratios of columnar ice crystals in a deep precipitating system over the Arctic observed by zenith-pointing Ka-band Doppler radar, *J. Appl. Meteorol. Climatol.*, *54*, 1060–1068.

Ryzhkov, A. V., S. E. Giangrande, A. Khain, M. Pinsky, and A. Pokrovsky (2008), Exploring model-based polarimetric retrieval of vertical profiles of precipitation, paper presented at 5th European Conference on Radar in Meteorology and Hydrology, Extended Abstracts, P6.1, FMI, Helsinki, Finland, 30 June – 4 July.

Ryzhkov, A. V., M. R. Kumjian, S. M. Ganson, and A. P. Khain (2013a), Polarimetric radar characteristics of melting hail. Part I: Theoretical simulations using spectral microphysical modeling, *J. Appl. Meteorol. Climatol.*, *52*, 2849–2870.

Ryzhkov, A. V., M. R. Kumjian, S. M. Ganson, and P. Zhang (2013b), Polarimetric radar characteristics of melting hail. Part II: Practical implications, *J. Appl. Meteorol. Climatol.*, *52*, 2871–2886.

Ryzhkov, A. V., M. Pinsky, A. Pokrovsky, and A. Khain (2011), Polarimetric radar observation operator for a cloud model with spectral microphysics, *J. Appl. Meteorol. Climatol.*, *50*, 873–894.

Ryzhkov, A. V., H. D. Reeves, J. Krause, and H. Burcham (2014a), Discrimination between winter precipitation types based on explicit microphysical modeling of melting and refreezing in the polarimetric hydrometeor classification algorithm, paper presented at 8th European Conference on Radar in Meteorology and Hydrology, DWD and DLR, Extended Abstracts, P07, MIC, Garmisch-Partenkirchen, Germany, 1–5 Sept.

Ryzhkov, A. V., T. J. Schuur, D. W. Burgess, P. L. Heinselman, S. E. Giangrande, and D. S. Zrnić (2005), The Joint Polarization Experiment: Polarimetric rainfall measurements and hydrometeor classification, *Bull. Am. Meteorol. Soc.*, *86*, 809–824.

Ryzhkov, A. V., P. Zhang, Q. Cao, S. Matrosov, V. Melnikov, and M. Knight (2014b), Measurements of circular depolarization ratio with the radar with simultaneous transmission/reception, paper presented at 8th European Conference on Radar in Meteorology and Hydrology, DWD and DLR, Extended Abstracts, Garmisch-Partenkirchen, Germany, 1–5 Sept.

Ryzhkov, A. V., P. Zhang, H. D. Reeves, M. R. Kumjian, T. Tschallener, S. Trömel, and C. Simmer (2016), Quasi-vertical profiles—A new way to look at polarimetric radar data, *J. Atmos. Oceanic Technol.*, doi:10.1175/JTECH-D-15-0020.1.

Schrom, R. S., M. R. Kumjian, and Y. Lu (2015), Polarimetric radar signatures of dendritic growth zones within Colorado winter storms, *J. Appl. Meteorol. Climatol.*, *54*, 2365–2388.

Schuur, T. J., A. V. Ryzhkov, and D. R. Clabo (2005), Climatological analysis of DSDs in Oklahoma as revealed by a 2D-video disdrometer and polarimetric WSR-88D, paper presented at 32nd Conf. on Radar Meteorology, Extended Abstracts, 15R.4, Am. Meteorol. Soc., Albuquerque, N. M., 24–28 Oct.

Stull, R. (2011), Wet-bulb temperature from relative humidity and air temperature, *J. Appl. Meteorol. Climatol.*, *50*, 2267–2269.

Sulia, K. J., and J. Y. Harrington (2011), Ice ascent ratio influences on mixed-phase clouds: Impacts on phase partitioning in parcel models, *J. Geophys. Res.*, *116*, D21309.

Szyrmer, W., and I. Zawadzki (1999), Modeling of the melting layer. Part I: Dynamics and microphysics, *J. Atmos. Sci.*, *56*, 3573–3592.

Szyrmer, W., and I. Zawadzki (2014), Snow studies. Part IV: Ensemble retrieval of snow microphysics from dual-wavelength vertically pointing radars, *J. Atmos. Sci.*, *71*, 1158–1170.

Trömel, S., M. R. Kumjian, A. V. Ryzhkov, C. Simmer, and M. Diederich (2013), Backscatter differential phase—Estimation and variability, *J. Appl. Meteorol. Climatol.*, *52*, 2529–2548.

Trömel, S., A. V. Ryzhkov, P. Zhang, and C. Simmer (2014), Investigations of backscatter differential phase in the melting layer, *J. Appl. Meteorol. Climatol.*, *53*, 2344–2359.

Vogel, J. M., F. Fabry, and I. Zawadzki (2015), Attempts to observe polarimetric signatures of riming in stratiform precipitation, paper presented at 37th Conf. on Radar Meteorology, Extended Abstracts, 6B.6, Am. Meteorol. Soc., Norman, Okla., 14–18 Sept.

Wang, J., X. Dong, and B. Xi (2015), Investigation of ice cloud microphysical properties of DCSs using aircraft in situ measurements during MC3E over the ARM SGP site, *J. Geophys. Res. Atmos.*, *120*, doi:10.1002/2014JD022795.

Williams, C. R. (2016), Reflectivity and liquid water content vertical decomposition diagrams to diagnose vertical evolution of raindrop size distributions, *J. Atmos. Oceanic Technol.*, doi:10.1175/JTECH-D-15-0208.1.

Yuter, S. E., and R. A. Houze (1995), Three-dimensional kinematic and microphysical evolution of Florida cumulonimbus. Part II: Frequency distributions of vertical velocity, reflectivity, and differential reflectivity, *Mon. Weather Rev.*, *123*, 1941–1963.

Zawadzki, I., W. Szyrmer, C. Bell, and F. Fabry (2005), Modeling of the melting layer. Part III: The density effect, *J. Atmos. Sci.*, *62*, 3705–3723.

Zhang, G., S. Luchs, A. V. Ryzhkov, M. Xue, L. Ryzhkova, and Q. Cao (2011), Winter precipitation microphysics characterized by polarimetric radar and video disdrometer observations in central Oklahoma, *J. Appl. Meteorol. Climatol.*, *50*, 1558–1570.

Zrnić, D. S., N. Balakrishnan, C. L. Ziegler, V. N. Bringi, K. Aydin, and T. Matejka (1993), Polarimetric signatures in the stratiform region of a mesoscale convective system, *J. Appl. Meteorol.*, *32*, 678–693.

Zrnić, D. S., and A. V. Ryzhkov (1999), Polarimetry for weather surveillance radars, *Bull. Am. Meteorol. Soc.*, *80*, 389–406.